Lithos 378–379 (2020) 105826

Contents lists available at ScienceDirect

Lithos

journal homepage: www.elsevier.com/locate/lithos

Research Article

Long-term storage of subduction-related volatiles in Northern Victoria Land lithospheric mantle: Insight from olivine-hosted melt inclusions from McMurdo basic lavas (Antarctica)

P.P. Giacomoni [a], C. Bonadiman [a], F. Casetta [a,*], B. Faccini [a], C. Ferlito [b], L. Ottolini [c], A. Zanetti [c], M. Coltorti [a,d]

[a] Department of Physics and Earth Sciences, University of Ferrara, Italy
[b] Department of Biological, Environmental and Geologic Sciences, University of Catania, Italy
[c] IGG-CNR, Section of Pavia, Italy
[d] INGV, Section of Palermo, Italy

ARTICLE INFO

Article history:
Received 30 April 2020
Received in revised form 2 September 2020
Accepted 2 October 2020
Available online 08 October 2020

Keywords:
Melt inclusions geochemistry
Mantle metasomatism
Volatiles budget
Ross subduction
Antarctica Cenozoic magmatism
Northern Victoria Land

ABSTRACT

H_2O, CO_2, F, Cl and S concentrations in olivine-hosted melt inclusions (MI) from Cenozoic alkaline volcanics of Northern Victoria Land (NVL, Antarctica) were determined by Secondary Ion Mass Spectrometry (SIMS). The most undegassed H_2O and CO_2 values varies from 1.14 to 2.64 wt% H_2O and from 2320 to 3900 ppm CO_2 for the least differentiated alkaline basalts and basanites, respectively. The same MI have F and Cl contents varying from 471 to 888 and from 474 to 1135 respectively, although some other MI can get up to 1377 of F and 1336 of Cl. A $H_2O/(H_2O + CO_2)$ molar ratios from 0.88 to 0.92 were determined, and taking into account the MI with the highest water content, a CO_2 content in the melts up to 4400 and 8800 ppm for basaltic and basanitic compositions were inferred. Assuming that these magmas were produced by about 3 to 7% of partial melting, the volatile content in the mantle sources were estimated and compared with the estimates obtained from amphibole-bearing mantle xenoliths abundantly entrained in the McMurdo basic lavas. The two approaches converge in obtaining the following values: $H_2O = 1160 \pm 436$ ppm; $CO_2 = 304 \pm 64$ ppm. Some discrepancies are observed for F and Cl, mainly due to the uncertainties in the F and Cl contents of amphibole and its modal content, both parameters spanning a rather large range.

The resulting CO_2/Nb and CO_2/Ba ratios are lower and H_2O/Ce higher than those estimated for Depleted MORB Mantle (DMM), suggesting that the NVL Cenozoic alkaline magmatism could be originated by an enriched mantle source composed by 60 to 70% Enriched Mantle (EM) and from 40 to 30% DMM.

A global comparison of fluid-related, highly incompatible and immobile/low incompatible elements such as Li, K, Cl, Ba, Nb, Dy and Yb allow to put forward that the prolonged (~500 to 100 Ma) Ross subduction event played a fundamental role in providing the volatile budget to the lithospheric mantle before the onset of the Cenozoic continental rifting.

1. Introduction

Volatile elements (H-C-O-F-Cl-S) deeply affect the mantle rheology and play a fundamental role in the genesis of basic magmas. Besides contributing to lower the mantle viscosity and its solidus and facilitating convective mechanisms, they drive the onset and extent of partial melting processes, ultimately affecting the composition of primary melts (Green 1973). At shallower levels, the volatiles content constraint the P-T condition of crystallization and magmatic fractionation of primary melts, ultimately determining the eruptive behavior of volcanic systems (Mollo et al., 2015; Giacomoni et al. 2018; Lanzafame et al. 2020). The prograde metamorphism of hydrated oceanic lithosphere triggers the segregation and migration of volatiles into the supra-subductive mantle wedge (Abers et al., 2006). In arc settings, part of these volatile components will be emitted in the atmosphere through volcanism, although a substantial portion could be dragged into the mantle transition zone (410–670 km) and/or at the core-mantle boundary at about 2900 km of depth. This extremely deep recycled volatile component could return to the surface through mid-ocean ridge (MORB), oceanic-island (OIB) and continental rift (Tucker et al. 2019).

Rheological and petrological studies have contributed in highlighting the complex interlink between the volatile circulation (primary and/or recycled) and plate tectonics since convection and simple non-Newtonian mantle behavior are not sufficient to provide the required toroidal motion for plate tectonic (Bercovici and Karato 2003; Abers et al., 2006). On the other hand, the recycling of volatiles (e.g., H_2O and CO_2) and their migration through intergranular boundaries seems to be

* Corresponding author.
E-mail address: cstfrc@unife.it (F. Casetta).

https://doi.org/10.1016/j.lithos.2020.105826
0024-4937/

necessary to achieve a self-lubricating state for mantle convection (Bercovici and Karato 2003). In this respect, the recycling of volatiles and the quantification of the global volatile cycle are key aspects for understanding the overall magmatic and thermal evolution of the planet. Moreover, the volatile fluxes from the mantle to the exosphere modulate Earth's atmosphere and climate on short and long-time scales and are critical to maintain the planet habitable (Dasgupta and Hirschmann, 2010; Dasgupta et al., 2010).

Although the role of recycled volatiles in subductive settings have been widely investigated (Zellmer et al., 2014), their long-term storage, effects on mantle convection and melting, as well as their role in the petrogenesis of intraplate and continental rift settings is still largely unknown. Petrological and experimental studies have revealed the importance of hydrated and/or carbonated solidus for the generation of alkaline magmas (Pilet et al. 2008). Schilling et al. (1980) were among the first to propose that "hot spots" could be also considered "wet spots", highlighting the importance of water in the punctual decompressional melting processes (e.g., Green 1973). In addition to H_2O, the presence of CO_2 and the coexistence of mantle heterogeneities and recycled crustal lithologies at mantle depth, may contribute to the melting anomalies observed in intraplate settings.

The complex tectonic processes responsible for the formation of continents, such as multiple accretions, contribute to the generation of intraplate magmatism by creating chemical heterogeneities in the lithospheric and sub-lithospheric mantle. Volatile-rich, metasomatized and/or eclogitic materials may develop gravitational instabilities that cause the higher density materials to sink into the convective mantle by lithospheric thinning, delamination or drip processes, introducing easily fusible material in the upper mantle (Elkins-Tanton 2007; Dasgupta et al., 2010).

The idea that continental flood basalts and continental rifting magmatism could be somehow linked to volatiles re-introduction in the mantle by previous subductive events was firstly drawn by Cox (1978) for the genesis of Karoo-Ferrar, Parana, Deccan and Columbia River Large Igneous Provinces (LIPs). A supporting evidence was recently provided by elemental and isotopic analyses of volatile in melt inclusions of primary composition (Ivanov et al. 2018; Stefano et al. 2011). To date, intimate relationships between the major magmatic rifting phases and the mobilization of alkali- and volatile-rich melts are worldwide recognized (e.g. Casetta et al. 2019). Subduction-related and intraplate LIPs can be distinguished on the basis of the Nb/La ratio of the erupted lavas. More recent studies on olivine- and cpx-hosted melt inclusions from Siberian Traps (Ivanov et al. 2018), Columbia River (Stefano et al. 2011), Basin and Range, Karoo, and Deccan evidenced that high (although variable) volatiles concentrations are associated to LIPs genesis. The investigation of these melt inclusions (MI) in phenocrysts from lavas of the Cenozoic East African and Rio Grande Rift highlighted the presence of a hydrated/carbonated sub-lithospheric domains in their mantle source, suggesting that the volatile-rich contents were the result of old subductions, namely the Pan-African (600–700 Ma) and the Laramide (80–40 Ma) respectively (Hudgins et al. 2015; Rowe et al. 2015).

The present study will contribute to this fascinating issue by investigating the major and trace element geochemistry and volatile content of olivine-hosted MIs from basaltic and basanitic lavas of the Cenozoic Western Antarctic Rift System (WARS) in Northern Victoria Land. These MIs can potentially preserve the chemical heterogeneities of the magma-forming source, since immediately after formation, they remain isolated from the surrounding uprising magma during differentiation (Danyushevsky et al., 2002). Thus, MI may represent one of the most powerful tools for analyzing the volatile (H_2O, CO_2, F, Cl and S) content of primary magmas, with the aim of understanding their origin and recycling in the mantle source/s. Their geochemical features will be also-compared with those of the metasomatic melts that were recognized in the Northern Victoria Land (NVL) Sub Continental Lithospheric Mantle (SCLM) thanks to a long series of investigations on ultramafic xenoliths carried onto the surface by alkaline lavas (Coltorti et al. 2004; Pelorosso et al. 2016, 2017; Perinelli et al. 2008). In this respect, and taking into account its complex tectono-magmatic evolution, NVL may represent an almost unique site where studying how subduction-related metasomatism and melt/fluid infiltration can be preserved within the lithospheric and sub-lithospheric mantle for hundreds million years before the production of rift-related alkaline magmas.

2. Geological outline

The WARS is one of the most extended rift systems on Earth, extending for about 3000 km, from the Ross Sea (Queen Maud Mountains-Northern Victoria Land) to the Weddell Sea (Whitmore-Horlick Mountains) and from 750 to 1000 km in width. It is the result of a complex geological process initiated about 550 Ma ago when East Antarctica was still part of the active Paleo-Pacific margin of Gondwana. The tectonic blocks constituting the West Antarctica were joined along the active margin with the Chatham Rise, Campbell Plateau, New Zealand and other crustal blocks collectively referred as Zeolandia (Salvini et al. 1997).

The Trans-Antarctic Mountains (TAM) constitutes the eastern flank of the WARS and are the uplifted roots (up to 4500 m high) of the early Paleozoic Ross Orogeny (480–550 My); here the Granite Harbor Intrusive suite provides the evidence for the inception of subduction-related magmatism by ~530 Ma (Rocchi et al., 2002). The Ross subduction continued, perhaps episodically, throughout the Mesozoic and began a progressive cessation from 110 to 94 Ma moving from the western to the eastern part of the Marie Byrd Land (MBL) (Mukasa and Dalziel 2000). From 550 Ma to 150 Ma before present, the Ross Orogeny was affected by extensive erosion and rifting before the onset of the Jurassic Ferrar magmatic event (182 $\pm$ 3 Ma), which covered 5 * 10^6 Km^2 with doleritic rocks. These large igneous events accompanied the Gondwana break-up, reasonably triggered by a plume headed on the South Africa-East Antarctica junction and culminated with the separation of Antarctica from South Africa (Rocchi et al., 2002). The initiation of the extension of the WARS occurred in the Cretaceous with the amagmatic opening of the Ross Sea embayment (Salvini et al. 1997), while rift-related magmatism initiated at about 48 and 30 Ma in NVL and MBL respectively (Rocchi et al., 2002)).

Previous explanations of the WARS magmatism included a single plume beneath MBL (Wörner, 1999) or a stratified source made up of the remnants of a plume head related to the Karoo LIP (Hole and LeMasurier, 1994; Panter et al., 2000). However, the shallow pervasive low-velocity anomaly underlying the WARS and extending beneath the rifted margins cannot be linked to a single thermally buoyant mantle plume. An alternative model suggests that Ross Cambrian-Cretaceous subductive event was responsible for the generation of the heterogeneous volatile-rich Cenozoic mantle source (Aviado et al. 2015; Panter et al. 2018). This model is also supported by the large isotopic variability ($^{87}Sr/^{86}Sr$; $^{143}Nd/^{144}Nd$; $^{206}Pb/^{204}Pb$; $^{207}Pb/^{204}Pb$; $^{208}Pb/^{204}Pb$; $\delta^{18}O$) which suggests heterogeneous source with recycled HIMU component superimposed to an hydrated (metasomatized) OIB-like sub-lithosphere domain (Aviado et al. 2015; Nardini et al. 2009). The recent study of Correale et al. (2019) shows an almost constant and low $^3He/^4He$ ratio of 7.1 $\pm$ 0.4 Ra in mantle minerals of xenoliths sampled in Baker Rocks, Greene Point and Handler Ridge; indicating the recycling of HIMU oceanic lithospheric component as an important process in the geologic evolution of NVL mantle. Recently, Panter et al. (2018) provided robust insights on the recycling of ancient subduction-related components, likely related to the long-lasting Ross subductive event (550–100 Ma), in the SCLM beneath West Antarctica. Indeed, whole rock Sr-Nd-Pb isotopes and $\delta^{18}O$ signature of olivine suggest that slab-derived carbonate-rich materials interacted with the West Antarctica SCLM at 100–80 Ma, generating enriched metasomes which then progressively melted during the magmatic phases connected to the WARS.

In the northernmost sector of the paleo-Pacific margin of NVL, three main tectonic domains coexist as accretion of distinct terranes. Moving

northwards, they are the Wilson Terrane, the Bowers Terrane and the Robertson Bay Terrane (Fig. 1). Cenozoic magmatism affected the NVL area since Eocene, resulting in the emplacement of plutons, dyke swarms and volcanoes in an area of about 400 × 80 km^2. The volcanic products were grouped in the McMurdo Volcanic Group, while intrusive and subvolcanic rocks are referred as Meander Intrusive Group. In the McMurdo Volcanic Group, basic lavas carry abundant ultramafic xenoliths, providing a useful source of information on the nature of the lithospheric mantle beneath the rift (Coltorti et al. 2004; Perinelli et al. 2008; Bonadiman et al. 2014; Pelorosso et al. 2016, 2017; Correale et al., 2019).

3. Sampling sites and analytical methods

Samples were collected during the XX (2004/2005) and XXVII (2011/2012) Italian Antarctic Expeditions at the Mario Zucchelli Base (Terra Nova Bay) and funded by Programma Nazionale Ricerca Antartide (PNRA). Olivine-phyric lavas come from three different NVL localities (Fig. 1), namely Shield Nunatak (74° 24′ 664″ S – 164° 30′ 511″E), Eldridge Bluff (73° 24′ 664′ S – 164° 40′ 833″ E) and Handler Ridge (72° 30′ 733″ S – 164° 40′ 833″ E). Shield Nunatak and Eldridge Bluff are both located in the Wilson Terrane but show very different geological and volcanological features. Shield Nunatak, located in the

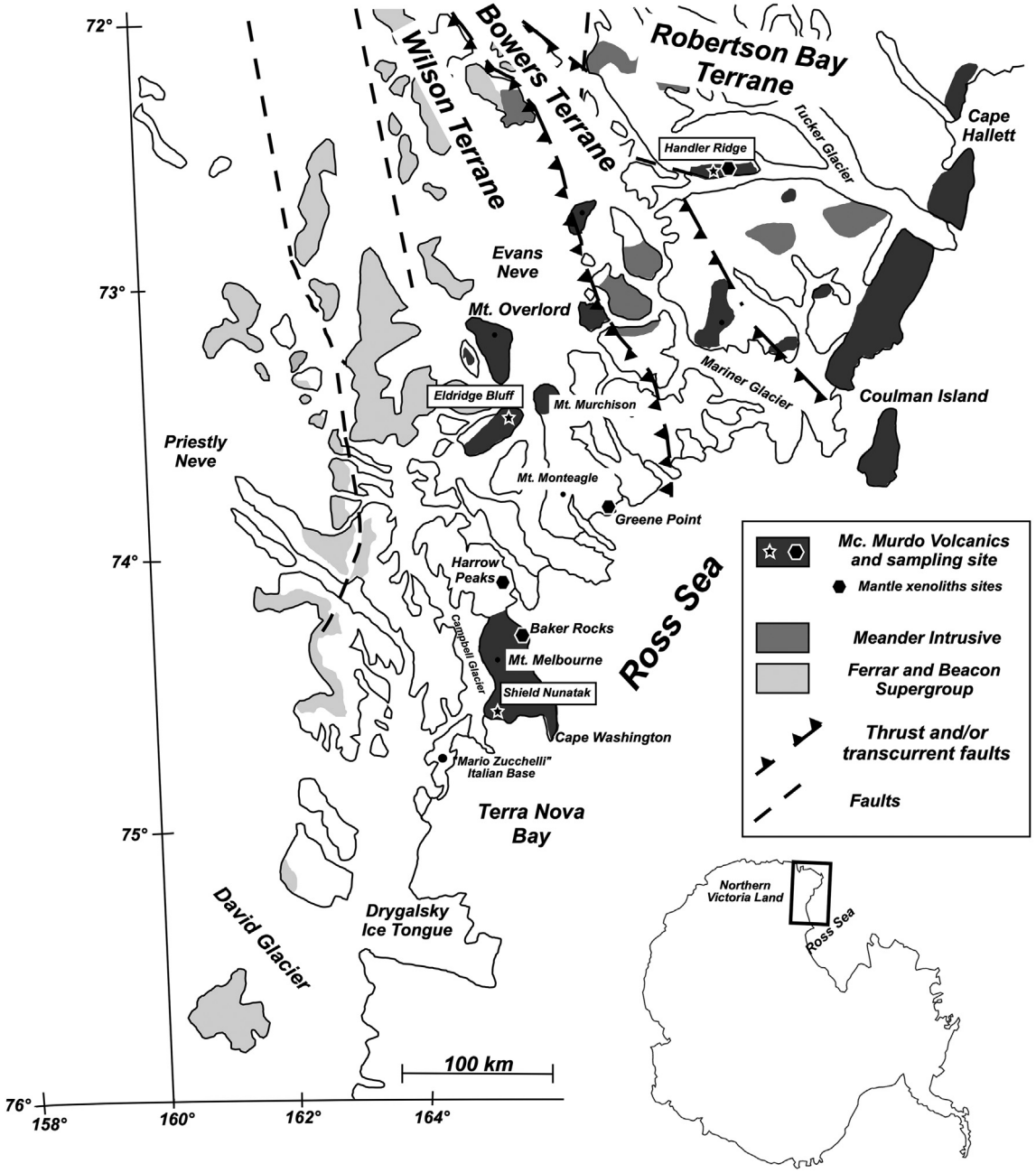

Fig. 1. Sketch geologic and tectonic map of Northern Victoria Land and its position on the Antarctica continent. Light grey represents the Jurassic Ferrar and Beacon Supergroup, Cenozoic Meander intrusive rocks and McMurdo volcanics are represented in dark grey and black respectively. Sampling site inside the McMurdo volcanics are indicated with stars (olivine-phyric basanite and basalts) and hexagons (mantle xenoliths).

Mt. Melbourne area, is a ~120 m high "nunatak" (Inselberg) inside the Campbell Glacier. This "nunatak" is composed by the survived remains of an extinct volcanic center dated 430 ± 82 ka (Giordano et al. 2012). Its stratified structure is made up by lava flows (which are the source of studied samples) and hyaloclastites at the base, grading to lava flows and welded pyroclastites at the top.

Eldridge Bluff is a ~1000 m high cliff boarding the Aviator Glacier. The complex stratified volcanic sequence that composes the cliff is made of lava flows and pyroclastites (basaltic lapilli, welded scoria and rare pyroclastic flows and surges), intruded by several basaltic dykes and sills. Samples were collected at the top of the cliff from a thick lava flow.

Handler Ridge is the northernmost sampling locality. This *E*-W elongated topography is part of the Victory Mountains, is located 50 km east of Cape Hallett Peninsula and extends for 10 km, parallel to the edge of the Trafalgar Glacier. At Handler Ridge, the meta-sedimentary sequence is intruded by several basanitic dykes culminating at the top with a series of aligned scoria cones, volcanic necks and lava flows attributable to the Cenozoic McMurdo Volcanic Group. The outcropping effusive products are olivine-phyric basanite with scarce clinopyroxene carrying abundant ultramafic nodules (Pelorosso et al. 2017), some crustal xenoliths and volcanic cognates.

3.1. Whole rock major and trace element analysis

Nineteen whole rock samples were cut into slabs, trimmed to remove the occasional surface alteration and subsequently crushed in a steel jaw and powdered in a rotary agate grinder.

The whole rock major and some trace elements (Ba, Cr, Sc, V, Nb, Y) concentration were determined by X-ray fluorescence (XRF – Thermo ARL Advant XP) using the correction method of Lachance and Trail (1966) on pressed pellets. Loss on ignition (L.O·I) was determined by gravimetric methods assuming Fe_2O_3 as 15% of FeO (Roeder and Emslie, 1970; Di Genova et al. 2016). Th, U, Rb, Zr, Sr and REE concentrations were measured by Inductively Coupled Plasma Mass Spectrometry (ICP-MS) on a VG Elemental Plasma Quad 2Plus instrument. The data reproducibility ranges between 0.9% and 7.9%. From a conservative point of view, it has been determined an accuracy of 10% and a detection limit of 10 ppb for Th, U and REE. Results are reported in Table 1.

3.2. Melt inclusion selection and re-homogenization

One hundred twenty-two (122) olivine grains from 600 μm to 2 mm in size were separated from crushed and sieved lava samples and individually inspected under binocular microscope to identify MIs. All grains were fresh, without any trace of weathering. Most MIs were crystalline with shrinkage bubbles, daughter clinopyroxenes and opaque minerals (magnetite and spinels), and separated fluid phases (Fig. 2a, b, c). Olivine crystals containing several distinct MIs with diameter greater than 50 μm were handpicked for analysis, whereas olivine grains displaying internal fracturing were discharged to avoid secondary effects such as volatile loss or gain. MIs homogenization process was achieved at Bruce Watson's Lab at Rensselaer Polytechnic Institute (NY-USA) using a piston cylinder apparatus. Ten to fifteen olivine grains were packed in a graphite powder and introduced in a graphite capsule to prevent the inclusion decrepitation during homogenization (technique and devise design Trail et al. 2012). Capsules were then brought to 6 kbar and 1300 °C in less than 1 min, held there for 10 min and quenched to below 200 °C within 20 s. According to Zhang and Stolper (1991) and Chen and Zhang (2008), under these conditions, homogenization occurs rapidly enough to preserve the MI bulk chemistry minimizing the volatile diffusion in or out of the system. Short time homogenization also prevents the contamination from the graphite capsule considering the low solubility and diffusivity of C in olivine, 0.1–1 ppm and $<10^{-12}$ cm^2/s respectively (Keppler et al. 2003; Shcheka et al. 2006). Recovered olivine grains were then mounted in epoxy resin and then ground and polished until melt inclusions were exposed (Fig. 2d, e). A petrographic observation of the mounts allowed us to identify and discharge inclusions with intersecting cracks.

3.3. Major element analyses of MIs and host olivines

Polished olivine grains mounts were then carbon coated and major and minor elements analyses of individual MI and host olivines were carried out by a Cameca SX100 Electron Microprobe (EMPA) at the IGG-CNR Lab of Padua (Italy). Measurements on MI were made with an accelerating voltage of 15 kV, a beam current of 10 nA, and a 5 μm defocused beam, while host olivines were analyzed with 15 kV acceleration voltage, 20 nA current and a 3 μm wide focused beam. The major element counting times were typically 20 s, while background counting times were half of the peak counting time. Detection limits were typically in the range of 0.02–0.06 wt%.

3.4. Measurements of volatile elements (H_2O, CO_2, F and Cl) in MIs

A selection of inclusions from Shield Nunatak were analyzed for the concentration of H_2O, CO_2, F, Cl and S with a Cameca 1280 IMS Secondary Ions Mass Spectrometry (SIMS) at the Woods Hole Oceanographic Institute (Massachusetts-USA). The rest of inclusions have been analyzed for H_2O, F and Cl concentrations by means of a Cameca 1280 IMS 4f ion microprobe installed at the C.N.R. Istituto di Georisorse (C.N.R.-I.G.G.) of Pavia (Italy). Selected olivine grains were previously re-polished to remove the carbon coating, detached from the epoxy mount and then pressed into an indium mount to improve the vacuum conditions during the analysis. The indium mount was then re-polished, washed and stored under vacuum prior to be gold coated. Secondary ions of ^{12}C, ^{16}O, ^{1}H, ^{19}F, ^{30}Si and ^{35}Cl were analyzed by a 10-μm wide $^{133}Cs^+$ primary ion beam with a 500 nA current and at 12.5 kV and ^{16}O primary-ion beam and current density of 1.5 nA at the Woods Hole Lab and IGG-CNR respectively (Ottolini et al. 2002). To eliminate any surface contamination, each spot analyzed was pre-sputtered for 240 s prior to analysis and then counted for a minimum of 10 cycles. A set of nine standards of volatile-bearing basaltic glasses (0.1–6.5% H_2O) was used for the calibration. Obtained SIMS data were reproducible within ±1% relative error.

3.5. Trace element analysis of MIs

Following SIMS analysis, olivine grains were polished and washed to remove the gold coating and Cs residuum before being analyzed by (LAM-ICP-MS) at the C.N.R.-I.G.G., Pavia (Italy). NIST 610 and NIST 612 standard glasses were used to calibrate relative element sensitivity and ^{43}Ca was used as an internal standard.

A laser spot size of 25 μm was used for smaller inclusions (<65 μm). The He carrier gas background signal for each analysis was measured for 60 s, at which time the laser was turned on and each inclusion was ablated for ~50–60 s. The precision and accuracy of trace element analyses were assessed by standard sample BCR-2 (reference values from USGS Geochemical Reference Materials Database).

The detection limit is a function of the ablation volume and counting time and is therefore calculated for each analysis; indeed, ablation volume greatly depends on instrument configuration. As a consequence, the detection limit is reduced if spot size, beam power and cell gas flow decrease.

3.6. Post-entrapment modification of MIs

The effects of post entrapment and re-heating on the chemistry of olivine-hosted MIs are well known (Danyushevsky et al. 2002). Due to cooling after entrapment, MIs are affected by various processes: crystallization, gaseous phase separation, shrinkage bubble formation or host olivine crystallization at the MI interface. This latter process may also

Table 1
Whole Rock Geochemistry of the studied samples from Northern Victoria Land (NVL). All trace elements were analyzed by means of ICP-MS except for V, Sc, Cr, Nb, Ba and Y (XRF). L.O.I. = Loss On Ignition; Mg# = MgO/(MgO + FeO) mol%.

Locality	Shield Nunatak										Eldridge Bluff		Handler Ridge				
Sample	CD172	CD173	CD174	CD175	CD176	CD177	CD178	CD179	CD180	CD181	CD281	CD282	HR2	HR4	HR5b	HR6b	HR7
SiO_2 (wt%)	45.54	45.86	46.32	45.69	45.37	46.06	45.50	45.46	44.04	45.25	46.48	45.13	42.99	43.85	42.78	42.63	42.07
TiO_2	2.96	2.89	2.87	2.95	2.89	2.81	2.86	2.86	3.06	3.01	2.13	2.04	3.64	3.50	3.61	3.63	3.70
Al_2O_3	14.87	14.25	14.41	14.51	14.73	14.68	14.73	13.40	13.38	14.26	14.80	14.56	12.63	12.46	12.32	14.78	14.64
Fe_2O_3	1.59	1.61	1.57	1.61	1.63	1.51	1.60	1.67	1.86	1.68	1.56	1.71	1.86	1.72	1.87	1.85	1.87
FeO	10.63	10.71	10.44	10.70	10.87	10.06	10.69	11.11	12.38	11.23	10.37	11.42	12.39	11.47	12.45	12.30	12.46
MnO	0.16	0.16	0.16	0.17	0.16	0.16	0.16	0.17	0.19	0.17	0.17	0.19	0.20	0.18	0.20	0.23	0.24
MgO	7.75	8.45	7.92	7.86	8.25	7.92	8.17	9.57	9.24	8.25	10.05	10.76	10.04	11.14	10.76	6.92	6.35
CaO	11.81	11.59	11.85	11.94	11.91	11.79	12.10	11.77	11.74	11.64	10.09	10.54	11.58	11.11	11.45	11.24	11.26
Na_2O	3.31	3.08	3.16	3.19	2.95	3.39	2.96	2.81	2.78	3.11	3.19	2.70	2.84	2.93	2.80	3.79	4.70
K_2O	0.76	0.73	0.73	0.77	0.72	0.78	0.70	0.69	0.81	0.78	0.78	0.70	1.43	1.18	1.37	1.51	1.55
P_2O_5	0.71	0.67	0.59	0.61	0.53	0.84	0.52	0.49	0.53	0.61	0.38	0.25	0.42	0.45	0.41	1.13	1.16
L.O.I.	0.51	1.03	0.31	0.47	0.52	0.99	0.42	0.40	0.75	0.62	1.02	0.89	1.16	0.75	1.02	0.37	1.22
Total	100	100	100	100	100	100	100	100	100	100	100	100	100	100	100	100	100
FeO_T	12.06	12.16	11.84	12.15	12.33	11.42	12.13	12.61	14.05	12.75	11.77	12.96	14.06	13.02	14.13	13.96	14.14
Mg#	56.41	58.35	57.40	56.60	57.40	58.28	57.56	60.45	56.98	56.60	63.23	62.60	58.99	63.31	60.53	49.96	47.48
Trace elements (ppm)																	
Rb	9.60	13.0	11.2	10.9	13.3	5.04	11.3	6.14	7.76	6.88	6.91	5.80	29.4	17.4	14.4	28.8	37.5
V	241	245	233	231	238	227	239	242	230	242	235	213	287	308	288	227	221
Sc	30.4	31.2	31.2	31.6	35.0	28.3	32.7	35.3	32.7	32.5	29.1	30.4	33.4	36.6	33.1	22.8	21.5
Cr	390	457	491	481	421	478	483	690	565	570	522	569	708	844	727	159	140
Sr	654	654	641	549	762	341	698	318	540	360	376	201	823	588	557	1053	1201
Th	1.70	3.71	2.40	2.20	2.59	2.71	2.98	1.46	2.85	1.62	1.24	0.84	6.44	5.12	4.28	8.32	8.02
U	1.22	1.34	1.1	0.84	1.00	0.80	1.22	0.67	1.20	0.93	0.53	0.59	1.60	1.40	1.40	2.22	2.51
Nb	38.6	40.0	39.4	40.7	38.0	38.0	35.6	35.1	36.7	38.9	27.1	25.1	72.3	68.0	71.2	103	111
Ba	313	313	311	317	303	256	296	283	283	299	241	212	509	521	508	618	609
Ta	2.99	3.10	2.51	2.04	2.54	1.87	2.19	1.45	2.21	1.82	1.82	1.49	1.12	0.96	1.17	1.44	1.60
La	32.9	34.2	29.4	30.8	37.0	19.6	32.6	17.1	28.6	19.5	19.2	11.0	51.5	43.4	44.8	75.3	77.2
Ce	51.2	55.3	48.7	47.9	77.5	41.7	68.6	36.1	63.0	41.9	41.9	25.0	103	90.2	93.9	152	149
Nd	31.1	92.8	27.8	29.3	42.0	22.1	36.5	20.4	32.2	22.7	20.5	11.8	45.2	38.8	40.2	67.4	67.9
Pr	18.4	22.0	19.4	20.5	9.64	5.07	8.46	4.63	7.41	5.19	4.86	2.77	10.85	9.26	9.78	16.45	16.25
Sm	9.15	9.4	8.89	8.54	8.56	6.42	7.29	4.26	6.36	4.67	4.16	2.41	8.33	7.11	7.31	11.9	11.8
Zr	167	235	166	173	259	162	239	135	258	198	192	140	213	174	213	336	361
Hf	6.10	5.23	5.80	5.60	8.14	5.11	6.61	4.48	7.14	5.93	5.55	4.47	4.59	3.84	4.61	6.56	7.00
Eu	2.11	2.54	2.05	1.99	3.02	1.79	2.49	1.46	2.13	1.54	1.39	0.80	2.60	2.22	2.28	3.49	3.44
Gd	5.99	6.1	5.78	4.67	7.82	4.00	6.42	3.93	5.72	4.17	3.95	2.31	7.42	6.20	6.43	10.5	10.3
Dy	5.56	5.6	4.88	4.9	5.36	2.62	4.28	2.81	3.71	2.83	2.98	1.77	4.91	4.00	4.08	6.63	6.54
Ho	0.99	1.03	0.78	0.98	0.98	0.48	0.78	0.52	0.68	0.52	0.58	0.35	0.87	0.71	0.72	1.18	1.16
Y	19.5	20.5	19.9	21.3	26.9	12.8	23.0	13.9	19.5	14.8	15.4	8.50	23.8	17.3	16.4	33.4	34.0
Er	1.55	1.65	1.34	1.58	2.38	1.15	1.87	1.25	1.62	1.25	1.47	0.88	2.17	1.74	1.75	2.89	2.85
Yb	1.22	1.38	1.04	0.99	1.79	0.83	1.34	0.94	1.13	0.89	1.22	0.72	1.89	1.45	1.46	2.42	2.44
Lu	0.16	0.17	0.11	0.13	0.25	0.12	0.19	0.13	0.16	0.12	0.18	0.10	0.24	0.18	0.18	0.31	0.32

occur during the re-heating homogenization procedure, that may also induce melting and enhance elemental diffusive mobility inward or outward the inclusion.

As a possible, important effect of post-entrapment crystallization (P.E.C.) of olivine onto the inclusion rims, is the fractionation of the incompatible species, including volatiles, in the remaining MI. To evaluate and correct this effect, olivine was incrementally added or subtracted, in 1 wt% steps, to or from an individual inclusion until each olivine-liquid (MI) pair had an $^{Ol\text{-}Liq.}Kd_{Fe/Mg}$ fitting the ideal value of 0.3 ± 0.03 (Roeder and Emslie, 1970). The data presentation and the following discussion will be exclusively referred to P.E.C. corrected inclusions. The correction percentages ranged from −16 to +10% (Tables 2a, 2b and 2c), where negative values reflect olivine added to the inclusion due to apparent overheating and assimilation of host olivine during re-homogenization (Danyushevsky et al. 2000) and positive numbers represent incomplete homogenization and sidewall crystallization.

4. Results

4.1. Petrography of lavas and MIs

All samples have a porphyritic texture with porphyritic indexes (P.I., defined as the percentage of phenocrysts with respect to the entire area of the thin section) in the range 10–15% for Handler Ridge and 20–30% for Eldridge Bluff and Shield Nunatak. All lavas have a common mineral assemblage made up of olivine (10–30%), clinopyroxene (5–15%), plagioclase (2–15%) and dispersed magnetite (2–7%), embedded in a glassy to hyalophilitic matrix. Rare apatite micro-phenocrysts were found in Shield Nunatak samples.

Olivine is the first liquidus phase in both basanitic and alkali basaltic samples, phenocrysts were euhedral, varying in size from 600 μm up to 2 mm. Olivine-hosted MI were rounded to slightly ovoidal in shape, varying from yellowish to brownish in colour and from 30 to 200 μm in size. Prior to homogenization MI varied from glassy to partially or fully crystalline with frequent shrinkage bubbles (Fig. 2), testifying the different cooling history of the magmas in the various localities. The morphology of daughter post-entrapment crystals varies from subspherical to elongate, rarely dendritic or spinifex while the mineral assemblage resembles that of the whole rock., with variable proportions of olivine, clinopyroxene and oxide phases (magnetite or Cr-spinel).

4.2. Major elements geochemistry of MIs and host olivines

Olivine phenocrysts range in forsterite [Fo = Mg/(Mg + Fe) * 100] values from 81.96 to 89.91 showing a quite large variability even within the same sample: from 81.96 to 86.24 in Shield Nunatak, from 78.84 to 86.58 in Eldridge Bluff and from 87.95 to 89.91 in Handler Ridge. An overall correlating trends between Mn and Ni contents and Fo are

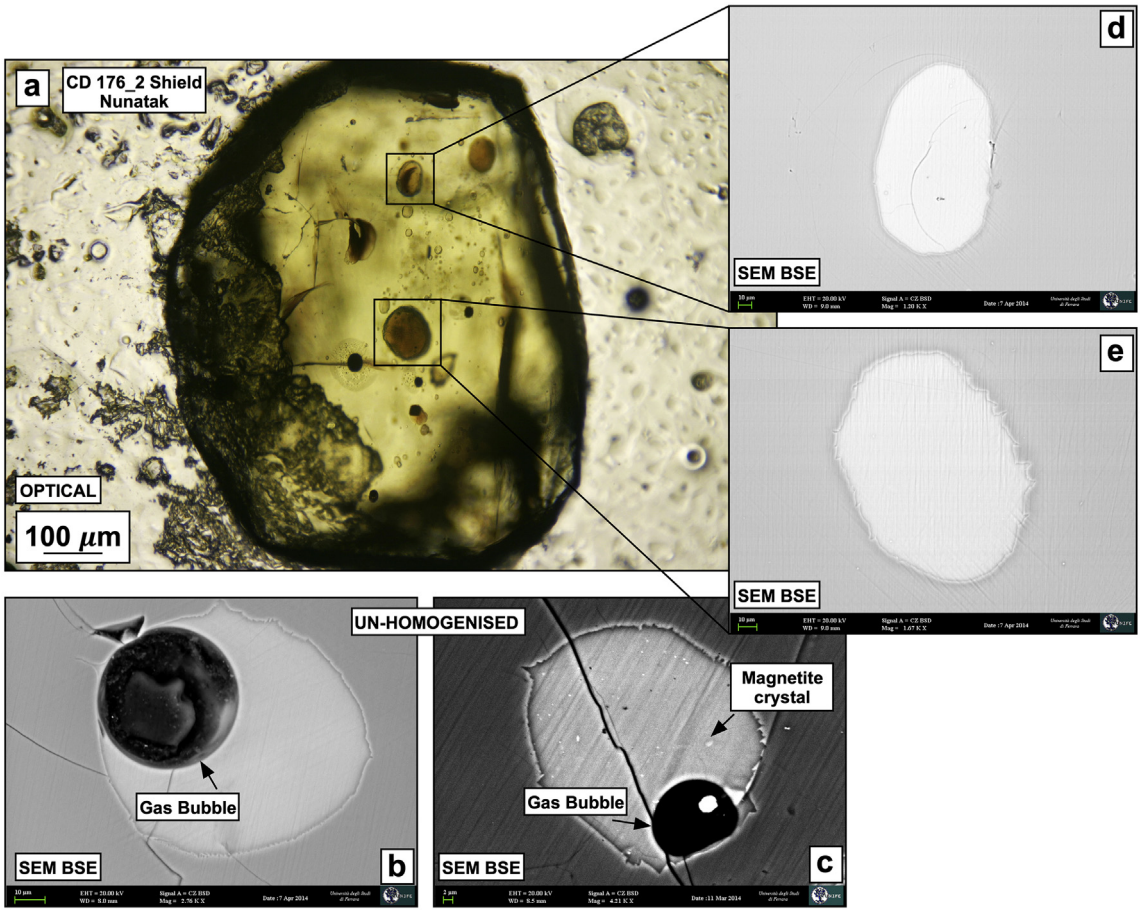

Fig. 2. Microphotographs of olivine phenocrysts hosting melt inclusions. a) Optical image of a millimetric size olivine from Shield Nunatak embedding two 50 μm wide melt inclusions; b) and c), Backscattered SEM images of un-homogenized inclusions with exsolved volatile bubbles and daughter magnetite crystals; d) and e), backscattered SEM images of melt inclusions after the homogenization procedure.

observed, as expected for olivine fractionation trend, although some phenocrysts show significant higher concentration of both elements (up to 3789 ppm and 2087 ppm for Ni and Mn respectively) at comparable Fo content. Ca concentration does not correlate with Fo showing a large variability in the same sample, ranging from 1072 to 3502 ppm. Chromium varies from 426 to 31.6 ppm with evident negative correlation with Fo, but remarkable internal variability.

On the total alkali vs silica diagram (TAS, Fig. 3a) the MI composition plot on the basanite and basalt fields, showing a quite larger variability with respect to the host lavas (Table 1) but overlapping the least differentiated products of the McMurdo Volcanic Group (Nardini et al. 2009). Dealing with glass composition is difficult to discriminate and correctly classify the MI, not having the opportunity to observe phenocrysts as for the lavas. The discrimination is mainly based on SiO_2, TiO_2 and incompatible element contents, although there are some clearly transitional analyses (Tables 2a, 2b and 2c). Some Shield Nunatak and Eldridge Bluff MIs for example plotting very close to the basanite-basalt line have been classified as basanites for their higher TiO_2 and incompatible element concentration. The SiO_2 concentrations vary from 42.38 to 44.98 wt% and from 45.41 to 48.28 wt%, while Mg# ($MgO/(MgO + FeO_T)$ mol%, ranges from 58.90 to 68.60 and from 58.14 to 65.54 for basanites and basalts respectively. On the whole the FeO_T, TiO_2 and CaO contents range from 8.51 to 15.23 wt%, from 4.19 to 1.42 wt% and from 6.38 to 13.94 respectively, showing a large variability in a restricted range of SiO_2 (Fig. 3b, c, d). K_2O contents vary from 0.35 to 1.57 wt% showing a peculiar negative trend with SiO_2 (Fig. 3e). Melt inclusions trapped in high-Fo olivine generally have lower SiO_2 and CaO contents encompassing the large variability even between MIs enclosed in the same olivine crystal. A similar consideration can be done for the FeO_T contents of the MI which generally decrease with the Fo of the host but can significantly vary in MI entrapped at comparable Fo.

4.3. Trace elements geochemistry of MIs

The primitive mantle (PM) normalized (McDonough and Sun 1995) incompatible trace elements patterns of melt inclusions strictly resemble those of the host lavas (Fig. 4a–c). Samples from each locality share a common large variability and a typical intraplate pattern enriched in large ion lithophile elements (LILE) with a variably marked negative anomalies of fluid mobile elements (Rb, U and Pb) and flat or slightly positive Ti anomaly. Basanitic lavas and MIs from Shield Nunatak and Eldridge Bluff have a higher concentration in LILE and REE. Basanitic MIs from Handler Ridge (Fig. 4c) differ from other localities by presenting a higher concentration in LILE, a less pronounced pattern of the highly incompatible elements (Rb—Ta) and a less marked U and Pb negative anomalies. La, Nb, and Zr in melt inclusions are negatively correlated with SiO_2 and positively correlated with MgO and Mg#, suggesting that they are not parental melts on the same liquid line of descent, but represent instead the entrapment of various melt produced by variable degree of partial melting that percolated through the mantle.

4.4. Volatile concentration of MIs

The entire H_2O and CO_2 concentrations in MI vary from 0.02 to 2.64 wt% and from 0 to 3900 ppm respectively. Despite the extensive degassing occurred in some MI, basanitic inclusions generally present

Table 2a
Geochemistry of melt inclusions from Shield Nunatak. Mg# = MgO/(MgO + FeO_T) mol%; P.E.C. = Post-Entrapment Crystallization.

Classification	Alkali Basalt				Basanite								
Sample	CD174-1-2	CD174-6-1_1	CD174-6-1_2	CD174-6-2	CD174-2	CD176-1-1	CD176-2-1_1	**CD176-2-1_2**	CD176-2-2_1	CD176-2-2_2	CD176-3-1_1	**CD176-4-1_1**	CD176B-9-1_1
SiO_2 (wt%)	46.51	47.06	47.30	47.20	44.07	43.30	44.19	**44.25**	44.39	44.03	44.24	**43.75**	43.60
TiO_2	2.74	3.24	3.10	3.48	3.53	3.37	3.00	**2.97**	2.95	2.95	2.98	**4.15**	3.35
Al_2O_3	15.73	13.36	13.74	15.57	13.42	11.41	12.75	**13.23**	12.87	12.96	13.31	**10.60**	12.65
FeO_T	10.46	10.78	10.84	9.64	9.64	15.15	10.53	**10.30**	10.11	10.03	11.14	**14.86**	14.11
MnO	0.16	0.20	0.18	0.13	0.22	0.21	0.19	**0.17**	0.18	0.14	0.18	**0.28**	0.22
MgO	8.18	10.05	9.72	6.83	13.94	12.29	12.95	**12.63**	13.36	13.37	12.52	**12.31**	11.39
CaO	10.90	12.12	11.83	12.82	11.78	8.38	11.72	**11.52**	11.23	11.35	11.28	**8.03**	10.48
Na_2O	3.26	2.09	2.04	2.98	2.27	3.45	2.19	**2.47**	2.55	2.64	2.81	**3.13**	2.73
K_2O	1.30	0.81	0.77	0.95	0.84	1.25	1.01	**1.09**	0.95	1.04	0.87	**1.43**	0.91
NiO	0.01	0.03	0.04	0.02	0.07	0.00	0.05	**0.03**	0.06	0.05	0.02	**0.01**	0.00
Cr_2O_3	0.00	0.07	0.07	0.07	0.05	0.00	0.04	**0.03**	0.08	0.07	0.06	**0.01**	0.04
P_2O_5	0.52	0.52	0.52	0.52	0.52	0.69	1.24	**1.17**	1.14	1.25	0.43	**1.24**	0.52
Total	99.8	100.3	100.2	100.2	100.3	99.5	99.9	**99.9**	99.9	99.9	99.9	**99.8**	100.0
P.E.C. corrected													
SiO_2 (wt%)	46.62	46.90	47.22	46.87	44.80	43.51	44.75	**44.82**	45.18	44.79	44.59	**43.84**	43.60
TiO_2	2.75	3.22	3.10	3.37	4.19	3.39	3.27	**3.24**	3.32	3.33	3.15	**4.16**	3.35
Al_2O_3	15.77	13.32	13.72	15.09	15.93	11.46	13.91	**14.42**	14.51	14.61	14.04	**10.62**	12.65
FeO_T	10.48	10.75	10.82	9.78	8.51	15.23	10.17	**9.92**	9.53	9.44	10.95	**14.89**	14.11
MnO	0.16	0.20	0.18	0.13	0.23	0.21	0.19	**0.17**	0.18	0.13	0.18	**0.28**	0.22
MgO	8.20	10.01	9.71	7.93	8.10	12.35	10.16	**9.82**	9.44	9.45	10.82	**12.33**	11.39
CaO	10.92	12.08	11.81	12.43	13.94	8.42	12.76	**12.53**	12.63	12.77	11.89	**8.05**	10.48
Na_2O	3.26	2.08	2.04	2.89	2.70	3.47	2.39	**2.69**	2.87	2.97	2.97	**3.13**	2.73
K_2O	1.30	0.81	0.77	0.92	0.99	1.26	1.10	**1.19**	1.07	1.17	0.92	**1.43**	0.91
NiO	0.01	0.03	0.04	0.02	0.03	0.00	0.04	**0.01**	0.05	0.03	0.01	**0.01**	0.00
Cr_2O_3	0.00	0.07	0.07	0.07	0.05	0.00	0.04	**0.03**	0.09	0.07	0.06	**0.01**	0.04
P_2O_5	0.53	0.52	0.52	0.50	0.52	0.69	1.23	**1.15**	1.13	1.24	0.43	**1.25**	0.52
Total	100	100	100	100	100	100	100	**100**	100	100	100	**100**	100
Mg#	58.14	62.32	61.43	59.00	62.82	59.01	63.95	**63.74**	63.75	64.00	63.68	**59.52**	58.90
P.E.C correction %	–	–	–	3	−16	–	−8	**−8**	−11	−11	−5	–	–
H_2O (wt%)	0.71	0.78	1.04	1.19	0.86	0.99	1.02	**1.19**	1.02	1.13	0.45	**2.64**	1.07
CO_2 (ppm)	26	128	131	341	1323	120	–	**3900**	350	–	–	–	300
F (ppm)	808	818	909	999	905	1377	868	**836**	835	904	923	**888**	1294
Cl (ppm)	570	492	443	510	1001	1068	1125	**1135**	1295	1032	1149	**810**	1224
$H_2O/(H_2O + CO_2)$	0.999	0.993	0.995	0.998	0.941	0.995		**0.882**	0.986				0.989
H_2O/Ce	74.6	148.8	201.8	199.5	141.8	97.2	80.9	**91.9**	83.4	92.2	81.0	243.4	164.3
Cl/F	0.71	0.60	0.49	0.51	1.11	0.78	1.30	**1.36**	1.55	1.14	1.24	**0.91**	0.95
Cl/K	0.05	0.07	0.07	0.06	0.12	0.10	0.12	**0.11**	0.14	0.10	0.15	**0.07**	0.16
Cl/Nb	13.0	13.7	12.0	13.8	34.4	17.8	22.1	**22.6**	26.6	19.5	29.9	**11.8**	30.3
Trace elements (ppm)													
Ni	332	312	302	356	270	406	278	**272**	322	300	341	**424**	316
V	170	223	239	231	244	179	271	**266**	304	302	286	**179**	235
Sc	28.6	26.7	24.7	32.5	34.8	18.5	31.3	**31.9**	27.9	31.6	30.1	**17.0**	29.2
Zn	138	122	171	180	226	256	131	**147**	131	152	133	**178**	138
Cr	19.6	452	499	554	393	39.9	301	**330**	279	333	124	**34.1**	106
Co	115	50.8	47.3	107	150	73.5	66.5	**65.6**	72.6	68.9	57.8	**61.8**	70.7
Li	35.4	46.1	38.6	40.1	33.9	23.5	42.2	**39.8**	32.2	35.6	33.2	**9.88**	64.6
Rb	28.7	15.8	20.4	20.6	10.7	32.1	25.5	**27.3**	27.6	26.7	19.5	**35.9**	17.0
Ba	296	264	253	280	372	448	457	**472**	451	448	433	**382**	469
Th	6.78	2.18	3.36	2.96	2.64	4.40	5.75	**5.52**	4.23	4.24	2.95	**5.64**	3.47
U	1.25	1.16	1.31	0.53	0.94	1.43	1.32	**1.24**	1.28	1.25	0.78	**1.56**	0.65
Nb	44.0	35.8	37.0	37.0	29.1	59.9	50.9	**50.2**	48.6	53.0	38.5	**68.6**	40.5
Ta	2.48	1.61	1.42	1.57	1.41	3.15	2.82	**2.62**	2.87	3.00	2.13	**3.92**	2.01
La	75.0	27.3	30.0	33.5	32.8	52.3	77.0	**79.1**	65.4	63.9	29.2	**55.6**	34.0

(continued on next page)

Table 2a (*continued*)

Classification	Alkali Basalt				Basanite								
Sample	CD174-1-2	CD174-6-1_1	CD174-6-1_2	CD174-6-2	CD174-2	CD176-1-1	CD176-2-1_1	**CD176-2-1_2**	CD176-2-2_1	CD176-2-2_2	CD176-3-1_1	**CD176-4-1_1**	CD176B-9-1_1
Ce	95.5	52.7	51.6	59.8	60.7	102	126	**129**	122	123	55.5	**108**	65.1
Pb	1.43	1.12	1.57	4.05	0.95	3.26	2.54	**2.96**	2.17	2.67	2.48	**2.61**	3.03
Sr	303	324	311	475	564	576	539	**550**	571	566	543	**503**	505
Nd	21.5	27.8	23.7	26.1	28.0	35.6	30.3	**38.8**	34.2	37.2	28.0	**55.3**	34.7
Pr	6.9	6.7	6.5	5.7	7.3	12.1	11.2	**11.2**	12.6	12.8	6.6	**12.7**	7.9
Sm	4.10	7.22	7.39	7.30	6.42	9.79	7.49	**6.40**	6.37	8.05	7.11	**11.4**	4.51
Zr	116	167	164	172	143	226	171	**169**	177	170	167	**273**	215
Hf	1.38	3.11	3.51	2.99	2.48	5.18	4.26	**3.46**	3.83	4.37	3.94	**6.31**	4.41
Eu	1.61	2.06	1.97	1.80	1.74	3.83	2.15	**1.86**	2.09	2.22	2.22	**3.80**	3.16
Gd	3.54	5.06	5.01	5.96	5.53	9.37	6.79	**4.60**	5.05	4.98	5.75	**9.52**	5.35
Dy	4.30	5.00	4.30	3.01	5.22	6.00	4.29	**4.30**	4.90	4.84	5.37	**6.10**	6.50
Ho	0.80	0.89	0.80	0.60	0.84	1.26	0.94	**0.70**	0.66	0.99	0.97	**1.39**	1.04
Y	14.8	21.0	23.1	18.5	21.0	32.4	20.6	**23.6**	22.2	23.2	21.8	**35.1**	24.7
Er	2.50	2.18	2.00	1.40	1.70	3.27	1.64	**1.60**	2.17	2.20	2.12	**3.24**	2.65
Yb	1.70	1.52	1.40	1.10	1.30	2.43	1.45	**1.11**	1.60	1.70	1.70	**2.65**	2.44
Lu	0.28	0.20	0.18	0.15	0.18	0.38	0.20	**0.18**	0.24	0.20	0.26	**0.40**	0.30

Table 2b
Geochemistry of melt inclusions from Eldridge Bluff. Mg# = MgO/(MgO + FeO_T) mol%; P.E.C. = Post-Entrapment Crystallization.

Classification	Basalt											Basanite					
Sample	CD281B-2-1_1	CD281B-2-1_2	CD281B-2-1_3	**CD281-2-4_1**	**CD281-4-1_1**	**CD281B-4-1_1**	CD281B-4-1_2	CD281B-5-1_1	CD281B-8-1_1	CD281B-8-1_2	CD281B-8-1_4	CD281-2-1_1	CD281-1-1_1	CD281-1-1_2	CD281B-6-1_1	CD281B-7-1_1	CD281-6-1_1
SiO_2 (wt%)	48.28	47.68	48.19	**45.41**	**47.18**	**45.89**	45.51	46.37	45.62	46.09	45.90	43.86	44.15	44.36	44.98	44.62	44.26
TiO_2	1.42	1.46	1.45	**2.39**	**2.57**	**2.01**	2.07	2.79	1.81	1.72	2.49	2.89	1.44	1.42	3.15	2.67	2.90
Al_2O_3	15.10	14.30	14.13	**11.97**	**12.45**	**14.43**	14.32	12.31	16.65	16.30	15.51	11.72	16.99	17.12	11.73	12.44	14.35
FeO_T	10.29	10.47	10.58	**13.67**	**11.19**	**10.89**	10.87	12.29	11.08	10.66	12.36	14.90	12.60	12.58	12.56	13.87	10.21
MnO	0.18	0.18	0.11	**0.21**	**0.16**	**0.16**	0.20	0.21	0.14	0.14	0.26	0.28	0.18	0.21	0.21	0.22	0.11
MgO	12.24	12.41	12.25	**13.25**	**12.80**	**11.43**	11.74	11.98	12.64	13.11	11.10	12.61	13.35	13.28	13.35	14.11	13.19
CaO	9.02	9.08	9.40	**9.15**	**9.64**	**11.12**	11.34	10.41	8.61	8.61	9.15	9.25	6.38	6.43	9.29	8.17	9.56
Na_2O	2.72	3.11	3.01	**2.80**	**2.59**	**2.97**	2.99	2.55	2.79	2.78	2.43	2.95	3.63	3.58	2.97	2.60	3.89
K_2O	0.47	0.43	0.48	**0.77**	**0.77**	**0.60**	0.61	0.66	0.56	0.51	0.35	0.69	0.96	0.82	1.03	0.44	0.85
NiO	0.03	0.00	0.04	**0.05**	**0.00**	**0.00**	0.02	0.03	0.01	0.00	0.04	0.00	0.05	0.01	0.01	0.04	0.09
Cr_2O_3	0.09	0.10	0.10	**0.01**	**0.04**	**0.04**	0.04	0.04	0.02	0.04	0.07	0.01	0.03	0.00	0.14	0.02	0.10
P_2O_5	0.19	0.19	0.18	**0.39**	**0.50**	**0.31**	0.29	0.39	0.12	0.08	0.33	0.48	0.23	0.20	0.58	0.48	0.49
Total	100.0	99.4	99.9	**100.1**	**99.9**	**99.8**	100.0	100.0	100.0	100.0	100.0	99.6	100.0	100.0	100.0	99.7	100.0
P.E.C. corrected																	
SiO_2 (wt%)	48.64	48.31	48.50	**45.38**	**47.88**	**46.19**	45.79	46.35	46.10	46.77	45.90	43.84	44.15	44.35	44.99	44.76	44.63
TiO_2	1.48	1.53	1.50	**2.39**	**2.77**	**2.07**	2.16	2.79	1.95	1.89	2.49	2.79	1.44	1.42	3.15	2.68	3.12
Al_2O_3	15.73	14.99	14.58	**11.96**	**13.41**	**14.91**	14.92	12.31	17.93	17.95	15.51	11.30	16.99	17.12	11.73	12.48	15.44
FeO_T	10.13	10.38	10.48	**13.66**	**10.88**	**10.76**	10.67	12.28	10.75	10.18	12.36	14.89	12.60	12.58	12.56	13.92	9.92
MnO	0.18	0.18	0.11	**0.21**	**0.15**	**0.16**	0.20	0.21	0.14	0.13	0.26	0.28	0.18	0.21	0.21	0.22	0.11
MgO	10.84	11.09	11.22	**13.24**	**10.38**	**10.40**	10.34	11.97	10.16	9.90	11.10	13.99	13.35	13.28	13.35	14.15	10.74
CaO	9.39	9.52	9.70	**9.14**	**10.37**	**11.48**	11.81	10.40	9.25	9.46	9.15	8.93	6.38	6.43	9.29	8.20	10.28
Na_2O	2.83	3.26	3.11	**2.80**	**2.79**	**3.06**	3.11	2.55	3.00	3.06	2.43	2.84	3.63	3.58	2.97	2.61	4.19
K_2O	0.49	0.45	0.50	**0.77**	**0.83**	**0.62**	0.64	0.66	0.60	0.56	0.35	0.67	0.96	0.82	1.03	0.44	0.92
NiO	0.02	0.01	0.03	**0.05**	**0.01**	**0.01**	0.01	0.03	0.01	0.02	0.04	0.01	0.05	0.01	0.01	0.04	0.07
Cr_2O_3	0.09	0.10	0.10	**0.01**	**0.04**	**0.04**	0.04	0.04	0.02	0.04	0.07	0.01	0.03	0.00	0.14	0.02	0.10
P_2O_5	0.19	0.19	0.18	**0.39**	**0.50**	**0.30**	0.29	0.39	0.12	0.08	0.33	0.46	0.23	0.20	0.58	0.48	0.49
Total	100	100	100	**100**	**100**	**100**	100	100	100	100	100	100	100	100	100	100	100
Mg#	65.52	65.47	65.54	**63.25**	**62.86**	**63.18**	63.24	63.37	62.66	63.33	61.46	62.52	65.29	65.21	65.35	64.36	65.79
P.E.C correction %	−4	−4	−3	–	**−7**	**−3**	−4	–	−7	−9	–	4	–	–	–	–	−7
H_2O (wt%)	0.58	–	–	**1.14**	**2.05**	**2.07**	0.46	0.49	–	–	–	1.39	0.47	1.21	2.34	–	0.38
CO_2 (ppm)	420	–	–	**2320**	–	–	120	76	–	–	–	–	210	–	–	–	–
F (ppm)	739	–	–	**471**	**445**	**464**	623	599	–	–	–	417	404	471	594	–	560
Cl (ppm)	501	–	–	**474**	**463**	**479**	682	482	–	–	–	988	416	1244	1098	–	971
$H_2O/(H_2O + CO_2)$	0.971			**0.923**			0.989	0.994					0.982				
H_2O/Ce	215.7			**242.1**	**417.5**	**515.8**	114.4	108.7				254.2	141.4	369.1	273.8		67.8
Cl/F	0.68			**1.01**	**1.04**	**1.03**	1.09	0.80				2.37	1.03	2.64	1.85		1.73
Cl/K	0.12			0.07	0.07	0.09	0.12	0.08				0.17	0.05	0.18	0.12		0.12
Cl/Nb	20.0			18.2	15.8	19.0	28.9	16.6				27.1	16.2	51.2	20.3		27.8
Trace elements (ppm)																	
Ni	99.0	92.0	102	**93.0**	**82.2**	**11.2**	21.0	52.0	91.0	85.0	105	55.6	110	107	99.0	95.0	119
V	163	185	164	**209**	**216**	**242**	231	253	145	132	145	210	137	141	185	206	264
Sc	22.9	23.9	27.7	**24.2**	**28.0**	**30.2**	31.1	28.0	30.1	19.8	28.4	27.3	11.0	11.6	24.3	23.4	29.6
Zn	105	92	98	**137**	**131**	**165**	229	130	181	139	103	161	167	179	204	233	127
Cr	647	560	640	**181**	**243**	**238**	212	286	347	337	346	286	333	336	532	295	551
Co	59.6	53.3	57.4	**57.6**	**40.8**	**20.3**	20.2	47.3	51.9	41.0	59.4	53.5	51.5	44.2	65.6	85.4	95.5
Li	29.8	26.6	33.3	**39.5**	**9.48**	**42.7**	40.9	35.2	37.8	49.4	9.5	30.9	12.2	13.3	22.2	32.4	18.4
Rb	3.31	5.25	3.00	**10.8**	**11.5**	**12.9**	12.5	12.1	8.75	4.31	3.80	11.3	20.3	19.8	16.3	9.4	20.9
Ba	149	226	206	**224**	**217**	**211**	236	221	235	236	195	316	168	322	375	287	313
Th	1.36	1.15	0.86	**2.17**	**2.31**	**1.41**	1.65	1.95	2.29	1.63	2.32	2.90	1.70	1.79	3.65	2.82	2.10
U	0.50	1.41	0.67	**0.41**	**0.46**	**0.76**	0.77	0.30	0.64	0.28	0.37	0.63	0.79	0.56	0.52	0.56	0.60
Nb	25.1	22.4	20.9	**26.1**	**29.3**	**25.2**	23.6	29.0	26.9	24.4	22.3	36.4	25.7	24.3	54.1	40.1	35.0
Ta	0.62	0.34	0.61	**1.48**	**1.56**	**1.36**	0.92	1.64	1.27	1.72	1.02	1.69	1.35	0.99	3.01	1.80	1.84

(continued on next page)

Table 2b (*continued*)

Classification	Basalt											Basanite					
Sample	CD281B-2-1_1	CD281B-2-1_2	CD281B-2-1_3	**CD281-2-4_1**	**CD281-4-1_1**	**CD281B-4-1_1**	CD281B-4-1_2	CD281B-5-1_1	CD281B-8-1_1	CD281B-8-1_2	CD281B-8-1_4	CD281-2-1_1	CD281-1-1_1	CD281-1-1_2	CD281B-6-1_1	CD281B-7-1_1	CD281-6-1_1
La	17.0	16.2	15.5	**24.5**	**25.7**	**19.7**	19.3	22.3	23.1	25.1	27.1	31.1	18.0	18.7	43.8	31.6	26.6
Ce	26.9	28.2	28.4	**47.1**	**49.1**	**40.1**	40.2	45.1	47.8	44.9	57.0	54.7	33.2	32.8	85.5	59.3	56.1
Pb	1.78	4.01	3.47	**1.95**	**1.76**	**2.46**	5.61	3.09	3.59	5.47	2.12	1.77	3.49	1.42	7.25	5.57	2.62
Sr	389	390	413	**398**	**383**	**379**	382	423	556	619	556	399	357	376	449	440	534
Nd	22.4	12.5	15.8	**24.1**	**25.2**	**22.5**	22.1	24.5	24.8	24.5	23.0	26.1	24.2	13.6	35.4	28.4	28.7
Pr	3.40	3.46	3.49	**5.87**	**6.18**	**4.28**	4.46	5.11	6.38	5.10	6.84	6.38	3.38	3.67	8.80	6.33	7.06
Sm	3.80	3.50	3.50	**4.58**	**6.11**	**5.22**	4.48	5.47	4.32	5.80	6.10	6.03	3.10	2.44	8.20	5.82	6.70
Zr	107	107	125	**135**	**144**	**189**	181	151	190	205	188	191	95.9	97.8	181	191	131
Hf	2.34	1.18	0.75	**2.54**	**3.25**	**2.97**	3.27	4.13	4.81	4.13	5.18	4.12	1.26	1.33	4.49	3.83	3.36
Eu	1.14	1.10	1.26	**2.12**	**2.10**	**1.80**	1.40	1.95	1.70	2.09	1.36	2.20	1.07	0.39	2.20	2.00	2.25
Gd	4.00	3.40	3.70	**5.54**	**5.87**	**3.60**	5.66	4.34	5.26	5.83	2.72	6.32	2.78	3.57	6.10	6.14	5.64
Dy	3.30	2.40	3.42	**4.31**	**4.30**	**4.30**	3.40	4.30	4.00	3.90	2.60	4.30	2.30	2.31	5.00	4.80	4.27
Ho	0.58	0.44	0.60	**0.79**	**0.97**	**0.81**	0.60	0.77	0.70	0.80	0.50	0.90	0.50	0.23	0.80	1.02	0.80
Y	13.9	11.2	15.5	**18.6**	**21.3**	**21.2**	21.2	20.8	19.0	22.6	21.3	22.9	14.4	14.8	34.6	22.8	19.9
Er	1.63	1.30	1.77	**1.82**	**1.88**	**2.09**	1.70	2.06	2.10	2.10	1.50	2.10	1.30	1.24	2.18	2.90	1.75
Yb	1.10	0.90	1.75	**1.60**	**1.90**	**1.70**	1.40	1.56	2.00	2.10	1.10	2.00	1.35	1.00	1.50	2.30	1.82
Lu	0.20	0.20	0.30	**0.23**	**0.30**	**0.20**	0.17	0.31	0.30	0.30	0.20	0.30	0.20	0.28	0.20	0.30	0.28

Table 2c
Geochemistry of melt inclusions from Handler Ridge. Mg# = MgO/(MgO + FeO_T) mol%; P.E.C. = Post-Entrapment Crystallization.

Classification	Basanite			
Sample	HR1-1-1	HR2-1-1	HR5-1-2	HR6-1-1
SiO_2 (wt%)	44.46	42.38	43.46	43.70
TiO_2	3.21	3.39	3.82	3.36
Al_2O_3	12.76	12.20	15.10	11.40
FeO_T	11.84	12.79	11.86	12.36
MnO	0.21	0.22	0.20	0.21
MgO	12.08	13.24	9.54	13.15
CaO	8.25	11.16	9.51	10.98
Na_2O	4.34	2.91	3.73	2.74
K_2O	1.61	0.76	1.65	1.06
NiO	0.00	0.00	0.01	0.00
Cr_2O_3	0.01	0.10	0.06	0.62
P_2O_5	0.79	0.42	0.65	0.42
Total	99.6	99.6	99.6	100.0
P.E.C. corrected				
SiO_2 (wt%)	44.53	42.40	43.31	43.60
TiO_2	3.13	3.18	3.49	3.26
Al_2O_3	12.43	11.45	13.78	11.06
FeO_T	11.88	12.70	11.88	12.33
MnO	0.21	0.22	0.20	0.21
MgO	13.19	15.63	13.06	14.18
CaO	8.05	10.48	8.69	10.66
Na_2O	4.23	2.72	3.40	2.66
K_2O	1.57	0.72	1.51	1.03
NiO	0.01	0.02	0.04	0.01
Cr_2O_3	0.01	0.10	0.06	0.60
P_2O_5	0.77	0.39	0.60	0.41
Total	100	100	100	100
Mg#	66.36	68.60	66.12	67.13
P.E.C. correction %	3	7	10	3
H_2O (wt%)	2.23	0.55	0.86	1.65
CO_2 (ppm)	–	57	–	–
F (ppm)	1280	967	1339	1015
Cl (ppm)	1296	940	1336	805
$H_2O/(H_2O + CO_2)$		0.996		
H_2O/Ce	195.9	62.5	97.2	206.2
Cl/F	1.01	0.97	1.00	0.79
Cl/K	0.10	0.15	0.10	0.09
Cl/Nb	16.3	16.2	21.9	16.0
Trace elements (ppm)				
Ni	224	253	237	235
V	187	285	199	293
Sc	19.2	27.5	15.2	31.5
Zn	290	144	139	132
Cr	563	604	368	4217
Co	199	49.0	60.7	24.7
Li	7.0	28.3	22.1	27.7
Rb	33.9	32.1	34.5	28.9
Ba	540	447	461	421
Th	7.19	4.25	4.27	3.89
U	1.61	1.29	1.33	1.17
Nb	79.3	58.0	61.0	50.2
Ta	4.30	3.05	3.16	2.72
La	64.0	48.3	52.1	45.3
Ce	113.8	88.0	88.5	80.0
Pb	9.08	2.68	8.29	2.65
Sr	818	769	767	741
Nd	51.3	40.9	40.9	39.2
Pr	12.5	10.0	9.77	9.37
Sm	8.68	8.00	9.14	8.88
Zr	181	159	149	150
Hf	4.61	3.81	2.58	3.53
Eu	2.85	2.50	2.80	2.52
Gd	6.38	6.49	4.41	6.48
Dy	4.92	4.37	3.65	4.43
Ho	1.09	0.83	0.71	0.76
Y	23.7	20.9	18.8	20.1
Er	2.43	1.65	1.79	1.70
Yb	1.79	1.66	1.46	1.40
Lu	0.25	0.24	0.20	0.22

a higher volatile concentration with respect to basaltic MI, and no correlation is observed with SiO_2 and alkalis, suggesting that the volatile contents are not dependent on melt fractionation (Fig. 5a–d; Tables 2a, 2b and 2c).

The relationship between H_2O and CO_2 suggest a different degassing paths of the melts in accordance with the lower solubility of CO_2 with respect to H_2O. Considering exclusively the most undegassed measured H_2O and CO_2 pairs (1.19 wt% – 3900 ppm; 1.14 wt% – 2320 ppm; Fig. 6), the original $H_2O/(H_2O + CO_2)$ molar ratios of 0.88 and 0.92 can be considered as minimum values for primary basanitic and basaltic melts respectively (Tables 2a, 2b and 2c; Fig. 6). Following these primary undegassed ratios, the primary concentration of CO_2 in the MI with the highest measured H_2O amounts, i.e. Shield Nunatak basanite with H_2O = 2.64 wt% and Eldridge Bluff basalt with H_2O = 2.07 wt%, have been estimated as 8800 and 4400 ppm, respectively. According to the solubility model of Papale et al. (2006), the highest CO_2 amount (3900 ppm) in MI was entrapped between 200 and 360 MPa, while MI with estimated 8800 ppm of CO_2 yield a minimum pressure of 650 MPa (Fig. 6).

These measured and estimated H_2O and CO_2 contents in MIs from NVL are consistent with those reported from the deep basanitic magma (DVDP) of Mt. Erebus (Oppenheimer et al. 2011), where the less degassed measured MI has 1.50 wt% H_2O and 5520 ppm CO_2 and a $(H_2O/H_2O + CO_2)$ molar ratio of ~0.86. These considerations lead us to retain that the CO_2 – flushing processes as not significant even if it cannot be excluded a priori. It has to be noted that, applying to the most H_2O-rich MI from NVL such a low molar ratio, the inferred primary CO_2 concentration would rise up to 10.000 ppm, a value very similar to that estimated by Tucker et al. (2019) for Hawaiian magmas.

The F and Cl contents measured in the MI range from 404 to 1377 ppm and from 416 to 1336 ppm respectively. No obvious trend between H_2O or CO_2 and F, Cl is observed, although with increasing F also Cl tends to increase. Basanitic MIs generally present a higher concentration of F and Cl (Fig. 5e, g) positively correlated with alkalis and with negligible or slightly negative correlation with SiO_2 (Fig. 5f, h). On the other hand, basaltic MIs show an increase in F both with respect to alkalis and SiO_2, while no variation can be observed as far as it concerns Cl. As a consequence, the F/Cl ratio has a substantial positive trend both with SiO_2 and alkalies.

5. Discussion

5.1. The volatiles' budget: from primary magmas to mantle source

The Primitive Mantle-normalized trace element patterns of basanitic and basaltic MI are well comparable, suggesting that they could have been generated by different partial melting degree of a similar source (Fig. 4). As above described the highest measured and estimated primary H_2O and CO_2 contents in basanitic MI are 2.64 wt% and 8800 ppm, respectively. Their corresponding F and Cl contents are 888 and 810 ppm, although some other basanitic MI can get up to 1377 and 1336 ppm of F and Cl, respectively. The same MI has Ba, Nb and Ce contents of 382, 68.6, and 108 ppm respectively. Analogously, alkali basaltic MI presents a measured and estimated primary H_2O, CO_2, F and Cl contents of 2.07 wt%, 4400, 464 and 479 ppm, respectively (Table 3), although within the group of basaltic MI F and Cl values can get up to 999 and 682 ppm respectively (Tables 2a, 2b and 2c). The same MI has Ba, Nb and Ce content of 211, 25.2, and 40.1 ppm respectively.

Assuming that a basanite and an alkali basalt could be produced from 3 to 7% of partial melting degrees (Green 1973) and that the four volatiles have a perfect incompatible behavior during melting, their

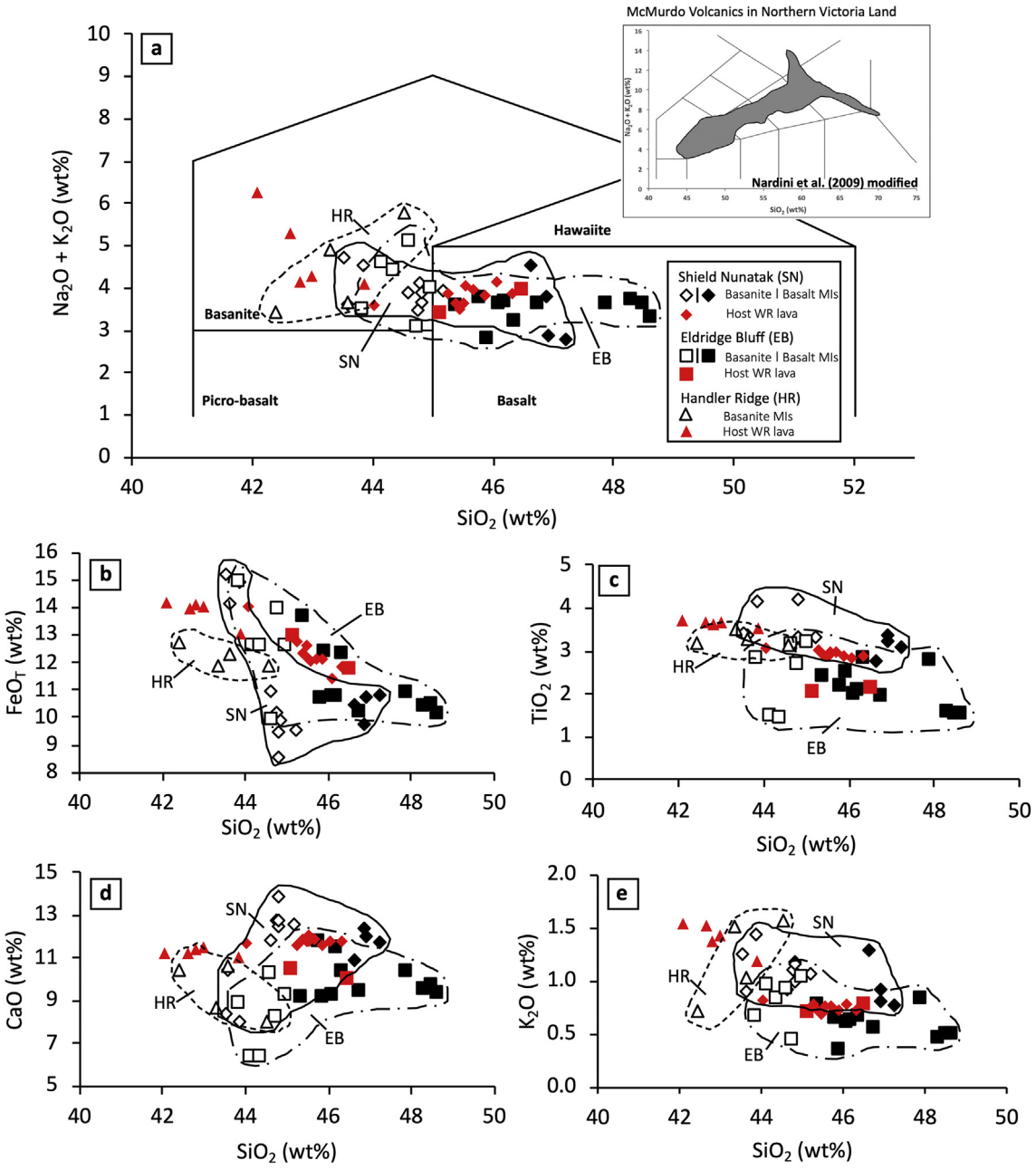

Fig. 3. Geochemistry of major element of host lavas (red symbols) and melt inclusions, black for basalts and white for basanites. a) Volcanic rock classification diagram (Le Bas et al. 1986). For comparison, light grey field show lavas of the entire McMurdo volcanic suite outcropping in Northern Victoria Land (Nardini et al. 2009). b) SiO_2 vs FeOt diagram; c) SiO_2 vs TiO_2 diagram; d) SiO_2 vs CaO diagram and e) SiO_2 vs K_2O. (For interpretation of the references to colour in this figure legend, the reader is referred to the web version of this article.)

concentration in the mantle source would be between 792 and 1449 ppm for H_2O (average 1121 ± 465), between 264 and 308 ppm for CO_2 (average 286 ± 31), between 26.7 and 32.5 ppm for F (average 29.6 ± 4.1) and between 24.3 and 33.5 ppm for Cl (average 28.9 ± 6.5) (Table 3). With the same rationality, the amounts of Ba, Nb and Ce in the mantle source that generated basanitic and basaltic melts were estimated as 11.5–14.7 ppm, 1.77–2.01 ppm, and 2.81–3.25 ppm, respectively (Table 3).

With these data and following Rosenthal et al. (2015) who established that CO_2 and Ba (and to a lesser extent Nb), have similar very incompatible partition coefficients, the CO_2/Ba, and CO_2/Nb of the mantle source can be calculated resulting in $CO_2/Ba = 22 \pm 1.5$ and $CO_2/Nb = 155 \pm 32.6$. These values are much lower than those estimated by Rosenthal et al. (2015) who found a CO_2/Ba and CO_2/Nb varying from 89 to 177 and from 337 to 673, respectively. The CO_2/Nb ratio of Antarctic MI appear somehow nearer to the lower end proposed by Saal et al. (2002) (193–285) but remains quite lower also with respect to the values proposed by Cartigny et al. (2008) (425–649) (Fig. 7).

These differences could be ascribed either to extensive pre-entrapment CO_2 degassing or to different primary mantle source composition. VolatileCalc (Newman and Lowenstern 2002) solubility model indicate that a basanitic melt with 8800 ppm of CO_2 at 1250 °C starts to exsolve CO_2 at 480 MPa. Since inclusions with 2.64 wt% H_2O and 8800 ppm CO_2 were trapped at >600 MPa (Papale et al. 2006; Fig. 6) it is likely to exclude the occurrence of extensive volatile exsolution prior to MI entrapment. Thus, the alternative explanation probably relies on the different nature of the inferred mantle sources. The Ba and Nb values used by Saal et al. (2002), Salters and Stracke (2004) and

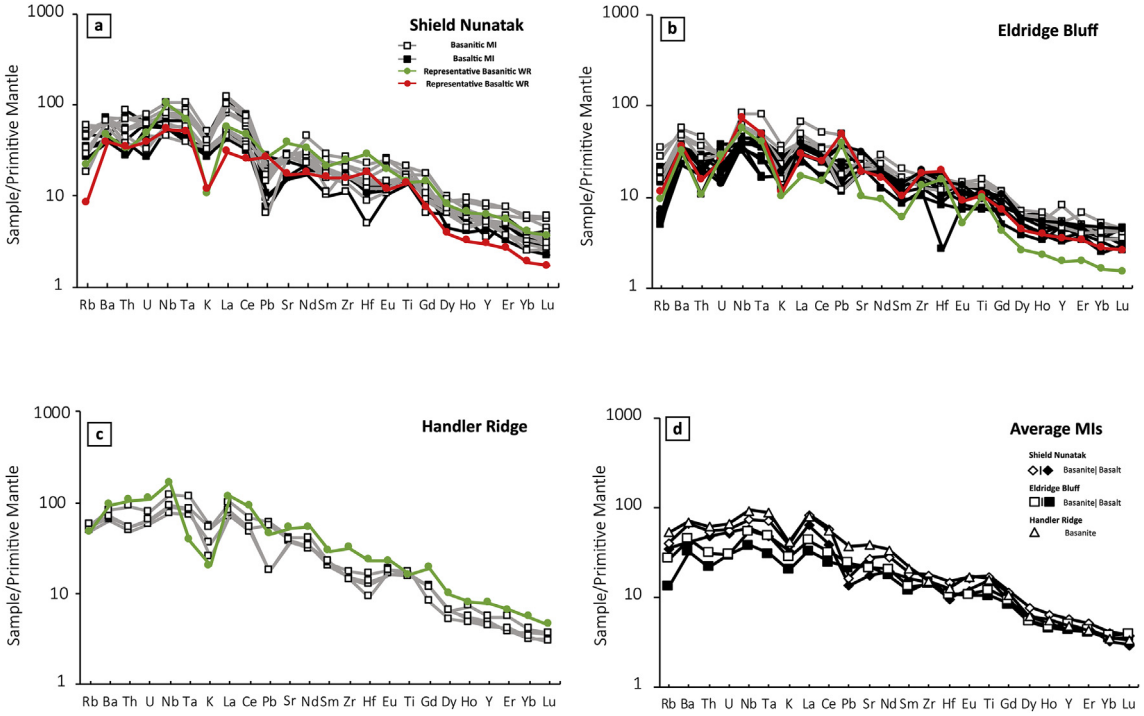

Fig. 4. Primitive mantle-normalized trace element distribution diagrams for melt inclusions and representative host-lavas from Shield Nunatak (a), Eldridge Bluff (b), Handler Ridge (c) and average values (d). Normalizing values from McDonough and Sun (1995).

Cartigny et al. (2008) in fact derived from the measured and estimated concentration on MORB and its related source (Workman and Hart 2005), and their estimated CO_2/Nb and CO_2/Ba ratios differ due to slightly CO_2 contents in the range of 45–100 ppm (Fig. 7). On the other hand, the calculated Ba and Nb contents of NVL mantle source are quite higher with respect to those estimated for the DMM (Ba = 0.56 and Nb = 0.15; Workman and Hart 2005). Supporting this statement is the variation of CO_2/Nb ratio from 10 to 77 in OIB settings such as Canary Islands, La Reunion, Hawaii (Longpré et al., 2017; Tucker et al. 2019; Walowsky et al., 2019) and Continental Rifts (i.e. East African Rift; Hudgins et al. 2015) to the 173–211 average ratios of MORB from the East Pacific Rise (Saal et al. 2002) and Gakkel Ridge (Shaw et al. 2010). The NVL MI plot between the low CO_2/Nb ratio of OIB and Continental Intraplate settings and the high ratio commonly found in MORB. This high variability could be ascribed on both mantle CO_2 and Nb heterogeneities, but we believe that for the Antarctic MI the enrichment in Ba and Nb of the source is causing the great variation in the CO_2/Ba and CO_2/Nb ratios, thus suggesting that primary melts have been generated by the melting of an enriched mantle source.

Similar comparison can be put forward for the H_2O/Ce ratio, which in NVL MI has a value of 377 ± 189, slightly higher than that of Cartigny et al. (2008) who estimated a range between 154 and 345 and Le Vojer et al., 2017 (245 ± 12). This represents an indirect confirm that most of the studied MI did not suffer significant H_2O loss prior to entrapment and testify the high H_2O content of both primary magmas and NVL mantle source.

5.2. The volatiles' budget: from mantle source to primary magmas

NVL Cenozoic basic magmas frequently contain mantle xenoliths, most of them with chemical and modal evidences of peridotite/melt interaction at mantle depths and potential relationships with the magmatic (alkaline) systems of WARS (Coltorti et al. 2004; Perinelli et al. 2008; Melchiorre et al. 2011; Bonadiman et al. 2014; Pelorosso et al. 2016, 2017). Mantle xenolith studies allow to set a direct link between the modal and chemical composition of this mantle domain, likely acquired during several melting and metasomatic/refertilization events, and the primary melts whose composition is mirrored by NVL MI. Although these xenoliths do not probably represent the composition of the mantle from which the magmas were derived, they could provide useful information on the nature and composition of the mantle domains below the WARS. The study of the two sides of a complex, but related geochemical system, allow to trace the volatile budget recycled and stored in the mantle, eventually entering in the primary magmas and MI.

Mantle xenoliths from Baker Rocks, Greene Point and Handler Ridge are spinel-bearing lherzolites and harzburgites, with modal amphibole as the only hydrated phase occurring at Baker Rocks as disseminated or in vein (5–15%). These amphiboles are formed from undersaturated alkali-silicate metasomatic fluids reacting with the pre-existing peridotitic mantle assemblage (Coltorti et al. 2004). In these peridotitic xenoliths, amphibole H_2O content up to 1.42 wt% was estimated by means of SIMS analyses (cfr. Table 3 in Bonadiman et al. 2014), while μ-FTIR measurements showed that the H_2O contents of nominally anhydrous minerals (NAMs) can be as high as hundreds of ppm (cfr. Table 1 in Bonadiman et al. 2009). The largest uncertainties in the following reasoning rely on i) the average modal composition of the amphibole-bearing mantle domains at Baker Rocks, where amphibole is present both disseminated and in veins, ii) on the preferential contribution of the veined amphibole during melting thus locally modifying both modal and eutectic composition and iii) the scarce number of analyses for constraining the volatile budget in mantle amphibole, together with its poorly known and highly variable partitioning coefficients of H_2O, F and Cl (Bizimis and Peslier 2015). Bearing in mind these limitations, a forward modelling to match the volatile content of the NVL MI has been tentatively developed, and some noteworthy results were obtained. The modal composition of the NVL SCLM has been taken from an average of about 50 xenoliths from Baker Rocks (Coltorti et al. 2020) and is reported in Table 4. The modal content of amphibole, which is the major volatiles repository, varies from 7 to 12%. Considering the average H_2O in amphibole measured by Bonadiman et al. (2014) as well as

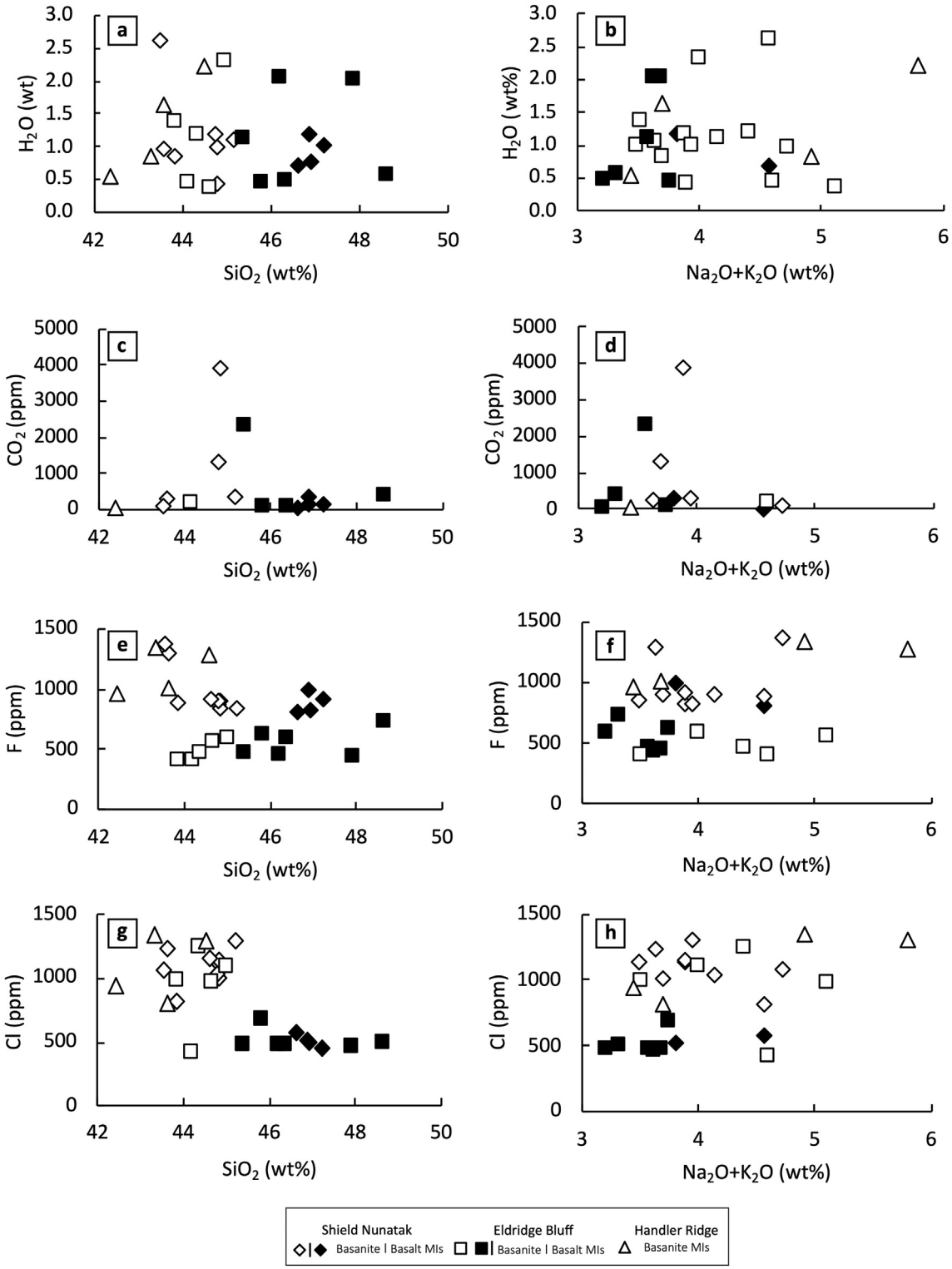

Fig. 5. Melt inclusions volatile elements distribution diagrams. a) SiO_2 vs H_2O; b) $Na_2O + K_2O$ vs H_2O; c) SiO_2 vs CO_2; d) $Na_2O + K_2O$ vs CO_2; e) SiO_2 vs F; f) $Na_2O + K_2O$ vs F; g) SiO_2 vs Cl; h) $Na_2O + K_2O$ vs Cl.

the H_2O contents in NAMs (Bonadiman et al. 2009) an average H_2O content of 1198 ± 407 ppm (910–1486 the whole variation range) can be estimated as representative of the SCLM beneath NVL (Table 4). This amount is well within the range recently estimated for other mantle domains, such as for the Subei Basin, Eastern China (328–1440 ppm; Hao et al. 2019).

Using the same approach and considering exclusively the modal and volatile content in the amphibole (Bonadiman et al. 2014), the F and Cl contents in the NVL lithospheric mantle source can be also calculated, bringing to an average F content of 184 ± 68 ppm (135–232 the whole variation range) and Cl content of 98 ± 37 ppm (72–124 the whole variation range).

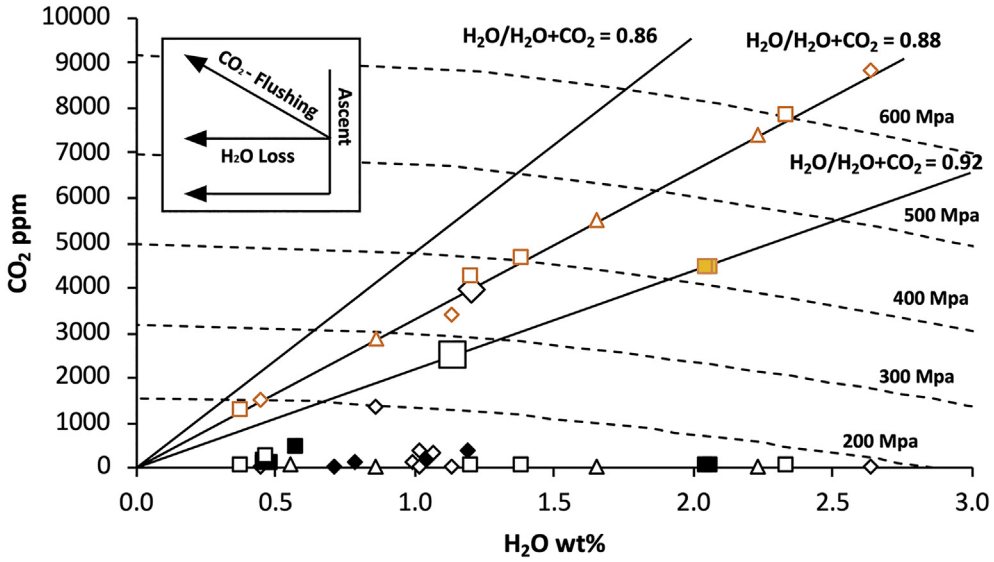

Fig. 6. CO_2 vs H_2O plot of analyzed melt inclusions. The $H_2O/(H_2O + CO_2)$ mol = 0.88, 0.92 lines are shown as representative of the primary undegassed ratios recognized for MIs with basanitic and basaltic composition respectively. The 0.86 ratio line is also plotted as representative of the composition recognized in Mt. Erebus melt inclusions from Oppenheimer et al. (2011). Full orange squares are the most hydrated basaltic inclusions with estimated CO_2 content along the 0.92 M ratio line. White symbols with orange outline are basanitic inclusions with estimated CO_2 content plotted along the 0.88 M ratio line. Isobars were calculated with the model of Papale et al. (2006). The effect of ascent, H_2O loss and CO_2 flushing are visualized by vectors, suggesting that H_2O loss during ascent is a fundamental process that affected the studied MIs.

By considering this inferred source as representative of the NVL SCLM, the non-modal batch melting model of Shaw (1979) (see also Table 4) was adopted for modelling the volatile budget of the hypothetical melts that can be generated from the mantle source. It is worth noticing that at 3 and 7% partial melting, the generated parental melts have H_2O concentrations of 1.6–3.2 and 1.0–2.4 wt%, respectively, well comparable to the ranges measured in basaltic and basanitic NVL MI. With the same approach, the modelled source is able to produce melts with 1184–2297 ppm of F and 965–2198 ppm of Cl or with 1306–2636 ppm of F and 1634–3245 ppm of Cl at 7 and 3% of partial melting, respectively. These values are however fairly higher on average than the F and Cl contents measured in NVL MI (up to 1377 ppm for F and 1339 for Cl), although a slight overlap appears in the lower end of the range. Altogether, these data suggest that 3 to 7% partial melting degree of an amphibole-bearing lherzolite from Baker Rocks are capable to reproduce the H_2O composition of basanitic and basaltic olivine-hosted MI. At the same time, however, our model indicates that the inferred amphibole involved in the genesis of Cenozoic alkaline melts at NVL was slightly depleted in F and Cl with respect to those reported by Bonadiman et al. (2014). Higher partial melting degree (up to 14%, Pelorosso et al. 2017) could be more feasible to fit the modelled F and Cl content in MIs but hardly acceptable for H_2O, CO_2 and the alkaline nature of melts. Moreover, partial melting

Table 3
Trace element and volatile concentrations in primary undegassed basanitic and basaltic melt inclusions and inferred composition of the related mantle source. CO_2 values in melt inclusions are calculated using $H_2O/(H_2O + CO_2)$ molar ratios of 0.88 and 0.92 (*) for basanite and basalt, respectively (see text for further explanations). The inferred composition of the mantle sources are calculated using the non-modal batch melting model of Shaw (1979) $C_0 = C_L \times F$, assuming a total incompatible behavior of all elements, thus considering the bulk partition coefficients D (source) and P (liquid) equal to zero. In this equation, C_0 represents the element concentration in the mantle source, C_L the element concentration in the melt inclusion and F the partial melting degree.

	Melt inclusions (MIs)		Inferred m antle source			
	Basanite	Basalt	From basanitic MIs	From basaltic MIs	Average	From xenoliths (Average)
Partial melting degree (F%)	0.03	0.07	–	–		
H_2O (wt%, ppm)	2.64	2.07	792	1449	1121 + 465	1198 ± 407[1]
CO_2 (ppm)	8800*	4400*	264	308	286 ± 31	322 ± 96 (This Study)
$H_2O/(H_2O + CO_2)$ mol	0.88	0.92	–	–		
F (ppm)	888	464	26.7	32.5	29.6 ± 4.1	184 ± 68[1]
Cl (ppm)	810	479	24.3	33.5	28.9 ± 6.5	98 ± 36[1]
Nb (ppm)	68.6	25.2	2.06	1.77	1.91 ± 0.21	–
Ba (ppm)	382	211	11.5	14.7	13.1 ± 2.3	–
Ce (ppm)	108	40.1	3.25	2.81	3.03 ± 0.31	–
CO_2/Nb	128	175	128	175	151 ± 32.6	–
CO_2/Ba	23.0	20.9	23.0	20.9	22 ± 1.5	–
H_2O/Ce	244	516	244	516	380 ± 193	–
Cartigny et al. (2008)	Primary melt		[1]Bonadiman et al. (2009)			
CO_2/Nb	425–649					
H_2O/Ce	154–345					
Rosenthal et al. (2015)						
CO_2/Nb	337–673					
CO_2/Ba	89–177					
Saal et al. (2002)						
CO_2/Nb	193–285					
Michael (1995)						
H_2O/Ce	155–280					

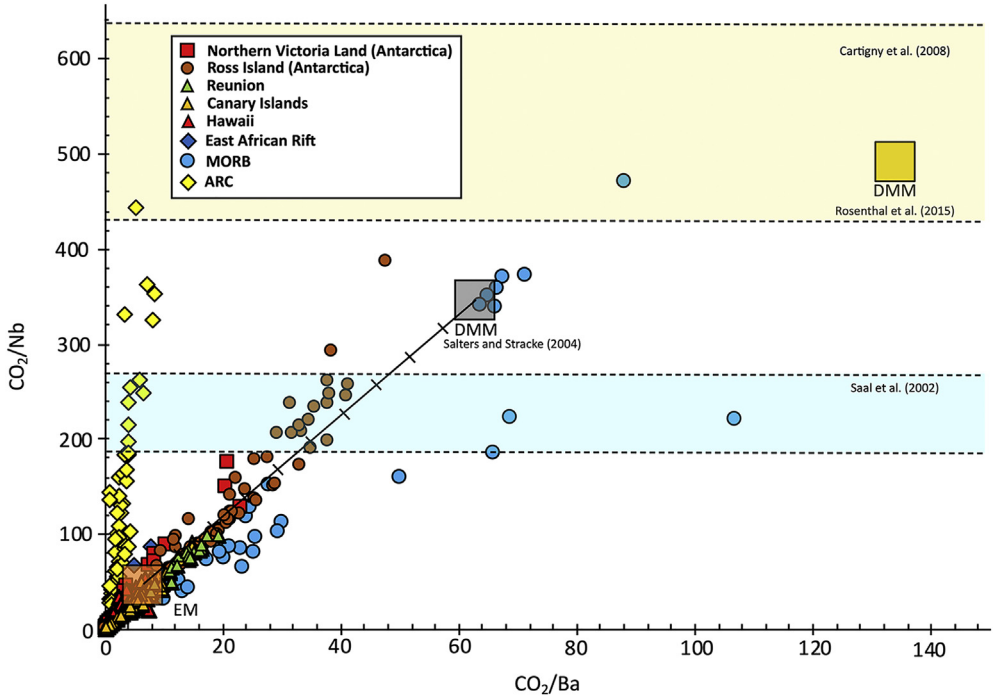

Fig. 7. CO_2/Nb versus CO_2/Ba of melt inclusions from NVL (This Study) in comparison with a literature dataset of melt inclusions composition from Ross Island, Antarctica (Rasmussen et al. 2017), Hawaii (Tucker et al. 2019), Reunion (Walowsky et al., 2019) and Canary Islands (Walowsky et al., 2019; Taracsak et al. 2019), MORB from East Pacific Rise (Le Roux et al., 2006), Gakkel Ridge (Shaw et al. 2010), ARC (Ruscitto et al. 2010; Johnson et al., 2008;Portnyagin et al., 2019), East African Rift (Hudgins et al. 2015). Depleted Morb Mantle (DMM) fields are derived from Salters and Stracke (2004) and Rosenthal et al. (2015) are shown for comparison while blue and yellow fields comprises the CO2/Nb of the DMM as calculated by Saal et al. (2002) and Cartigny et al. (2008) respectively. The composition of Enriched Mantle (EM) composition has been obtained from Casetta et al. (2019) in accordance with an estimate of 300 ppm CO_2 in the source. The graduated line model the linear mixing between the EM source and the DMM of Salters and Stracke (2004), suggesting that studied Mis from NVL could be originated by a mantle source made of 70% EM – 30% DMM. (For interpretation of the references to colour in this figure legend, the reader is referred to the web version of this article.)

episode/s recorded by the mantle are not univocally linked to the petrogenesis of the basalts that entrap the xenoliths.

Finally, by considering the $H_2O/(H_2O + CO_2)$ molar ratio of 0.88 and 0.92 measured in the MI a CO_2 content of 254–390 ppm (average 322 ± 96) can be derived from the amount of H_2O inferred in the mantle source. Such CO_2 concentration well fits the range calculated using the backward approach from the basaltic and basanitic MIs at 7 and 3% partial melting, respectively (Table 4).

5.3. Geodynamic implications of NVL volatile budget

The origin and concentration of volatiles on Earth are a debated topic since the pioneering study of Robey (1951) who proposed that oceans could not be derived from the alteration of rocks on the Earth surface. After that, many studies investigated the origin and concentration of terrestrial volatiles often using noble gases as physical tracers (Marty, 2012 and reference therein). The measured concentration of volatiles

Table 4
Modal composition and volatile content (H_2O, F, Cl) of the lherzolitic mantle source and relative mineral assemblage used in the partial melting models. The modal composition and variability of the lherzolite, as well as the volatile concentration in the mineral phases are based on real observations and determinations made on mantle xenoliths from Baker Rocks (Bonadiman et al. 2009, 2014; Coltorti et al. 2004). Volatiles concentrations in the mantle source (C_0) are calculated as weighted mean of the mineral phases. Volatiles concentration in the basanitic and basaltic melts are calculated from the non-modal batch melting equation of Shaw (1979) $C_L = C_0/[D + F * (1\text{-}P)]$. C_L = volatile concentration in the produced melt; C_0 = volatile concentration in the lherzolitic source; P = partition coefficient obtained weighted for the eutectic mineral melting proportions; F = partial melting degree; D = partition coefficient weighted for the modal composition of the source. Mineral phase eutectic melting proportions and partition coefficients (with corresponding references) used in the partial melting models are also shown.

	Modal composition (vol%)		Eutectic melting proportions			Mineral phase volatiles concentration (ppm)				Partition coefficients		
						H_2O	F	Cl	CO_2	H_2O	F	Cl
Olivine	63–63.5		0			30	0	0	–	0.004	0	0.003
Orthopyroxene	15–18		0			166	0	0	–	0.006	0.12	6E-04
Clinopyroxene	8.5–10.0		0.2			399	0	0	–	0.012	0.15	0.006
Spinel	1.0–2.0		0.05			0	0	0	–	0	0	0
Amphibole	7.0–12.0		0.75			11,733	1933	1033	–	0.243	0.43	0.119
					C_0 (ppm)	910–1486	135–232	72–124	254–390			
	C_L					Maximum amounts determined in MIs						
Melt composition and partial melting degree (F)	H_2O (wt%)	F (ppm)	Cl (ppm)	CO_2 (ppm)		H_2O (wt%)	F (ppm)	Cl (ppm)	CO_2 (ppm)			
Basanite (3%)	1.00–2.38	1306–2636	1634–3245	5571–13,000		2.64	1377	1339	8800			
Basalt (7%)	1.57–3.21	1184–2297	965–2198	3629–8467		2.07	999	682	4400			

H_2O: olivine, orthopyroxene, clinopyroxene and spinel partition coefficients are from Novella et al. (2014); amphibole partition coefficient is from Hauri et al. (2006).
F, Cl: all partition coefficients are from Dalou et al. (2014).

in primary MIs and the estimated amount in mantle source of the WARS magmatism are thus important proxies that must be contextualized in the frame of the well-known mantle geochemical reservoirs: Depleted Mantle (DM), Upper Mantle (UM), the Bulk Silicate Earth (BSE) and the Enriched Mantle (EM) end members.

The H_2O abundances of DM were estimated most entirely from measurements of H_2O contents in bulk rocks or glass inclusions of MORB-type magmas which erupted at sufficient ocean depth to prevent significant H_2O degassing. The preferred range is 150 ± 50 ppm of H_2O in DM (Saal et al. 2002; Marty et al., 2012). Current estimates of water contents in the UM (as source of the Earth's whole magmatism) rely on a combination of MORB and OIB material, mantle xenoliths, as well as on cosmochemical and geochemical arguments. Global estimates converge to 250–1000 ppm of H_2O in UM, while BSE is geochemically constrained to contain between 800 and 2400 ppm H_2O (Hirschmann and Dasgupta 2009; Marty 2012).

In this context, the H_2O estimated values for the WARS mantle source, from both backward calculations from water concentration in MI (1121 ± 465 ppm; Table 3) and forward approach by mass balance models from mantle xenoliths (1198 ± 407 ppm) is drawing close to the upper limit of the Upper Mantle or, conversely, to the lower limits of the BSE. On the other hand, the C inventory of DM, UM and BSE reservoirs have been estimated by means of the $^3He/^4He$, ^{40}Ar and N flux calibrations (Marty et al., 2012). The earliest C proposed value of 50 ± 25 ppm (Marty and Zimmermann 1999) for DM is enclosed in a large distribution of values, which lie between 30 ± 10 ppm for N-MORB to 140 ± 30 ppm for more enriched *E*-MORB mantle. More recently, various authors (Hirschmann and Dasgupta 2009; Salters and Stracke 2004), combining measurements of volatile fluxes at the oceanic surface with C measurements of olivine-hosted MI, obtained remarkably lower values (16 ± 9 ppm).

A more recently determined C range of 38–327 ppm (Marty 2012; Miller et al. 2019) reflects the extent of heterogeneity of C concentration in the upper mantle and demonstrates that mantle source composition is an important contributor to the geographical and temporal variations in the Earth's surface CO_2 fluxes.

The BSE carbon inventory is reconstructed by carbon estimates of DM-UM mantle reservoirs, inferring, from geochemical mass balance, the size of the deep mantle reservoir, and using the carbon-gas or carbon-trace element ratios (Marty 2012). Argon isotope budgets across all Earth's reservoirs, along with volatile ratios (C/N and $C/^4He$), provide a C estimates of the BSE in the narrow range of 671–772 ppm (Marty 2012; Miller et al. 2019). Applying the carbon/incompatible trace element (C/ITE) bulk model, Hirschmann (2018) estimated that BSE can contain 140 ± 44 ppm C. This model assumes that all oceanic basalts preserve similar C/ITE ratios in their mantle reservoirs. This assumption is in evident contrast with observed large C/ITE variability in OIB and most of alkaline basic magmas (GEOROCK database), which suggest the existence of variably enriched mantle reservoirs.

In this frame, our estimated CO_2 concentration in the WARS mantle source (~286 ± 31 using the backward approach from MI, 322 ± 96 ppm using the water amount of the SCLM inferred from xenoliths) plots near the upper limit of the proposed UM modelled CO_2, showing the same behavior as for H_2O. It is worth noticing that this result is strongly dependent on the assumption of a $H_2O/(H_2O + CO_2)$ mol = 0.88–0.92, and therefore should be considered as highly conservative. Indeed, compared with the estimated CO_2 concentrations for other alkaline magmas associated to enriched mantle domains, our result appears significantly lower, plotting well below the bulk mantle C determination of 600 ± 200 ppm (Marty 2012; Miller et al. 2019).

An alternative model has been suggested by Rosenthal et al. (2015), who proposed that a mantle source constituted by OIB-like enriched and DMM components can retain from 130 ± 30 ppm CO_2 (30% OIB + 70% DMM) to 440 ± 140 ppm CO_2 (90% OIB + 10% DMM). This value is also in accordance with what observed by Tucker et al. (2019) at Loihi and Highest Mauna Loa volcanoes in Hawaii, and their estimated mantle CO_2 concentration between 380 and 440 ppm is not so far from the values obtained in our models. In our case a mixed mantle source made up of 60–79% EM and 30–40% DMM (Salters and Stracke 2004, Fig. 7) will account for both the CO_2, as well as the Nb (1.91 ± 0.21) and Ce (3.03 ± 0.31 ppm) contents. Indeed, such a mixed source will be more enriched than DMM and PM end-members (Workman and Hart 2005), but slightly more depleted than the EM source inferred for other intra-continental magmatic domains (Casetta et al. 2020).

5.4. Are fluids related to the Ross subductive event?

With the aim to speculate about the relationship between the volatiles concentration in WARS magmas and the major geodynamic processes that in time and space were able to mobilize such elements in the Antarctic area (i.e. Ross Orogeny subduction started 550 Ma), various fluid-related geochemical tracers were examined. This brought to the comparison between NVL samples and representative magmas generated from active convergent settings and/or from mantle source which experienced ancient (>100 Ma) subduction-related modifications.

The ratio of Li/Yb, for example, is a proxy to trace the presence of a fluid derived by the de-hydration of sediments in the subductive slab (Liu and Rudnick 2011). Li and Yb are both lithophile elements, but the former is a soluble light element (as Na, Ca and Mg) and moderately incompatible during melting and crystallization (bulk D_{Li} for MORB and OIB 0.25–0.35), whereas the latter is an insoluble heavy element. The WARS MI have Li/Yb in the range of 3 to 36, extending far beyond the values of MORB (up to 1.8 Li/Yb) and OIB (up to 2.3 Li/Yb) (Arevalo and McDonough 2010; Chan and Kastner 2000). In the Li/Yb vs Dy/Yb plot (Fig. 8) the NVL MI form an array crossing the global subducted sediments field (GLOSS-II; Plank 2014) toward values similar to those found in-porous fluid films and clay-rich sediments in subductive settings (Chan and Kastner 2000; Nyakairu and Koeberl 2001).

Cl content is also a good candidate to trace if the mantle source of the WARS has been metasomatized by subduction-related fluids and/or hydrous melts (Broadley et al. 2016). In fact, Cl due to its higher solubility in basaltic melts, represents a minor component in the vapor phase (Rowe and Lassiter 2009). Rowe and Lassiter (2009), argued that Cl behaves as a highly incompatible element below saturation, being more incompatible than K and similar in compatibility to Nb, thus making the Cl/K and Cl/Nb ratios in primary magmas (or MI) representative of mantle source values. Since Nb, in contrast to K, is not mobilized by aqueous fluids, the Cl/Nb ratio is very sensitive to Cl enrichment by subduction-related fluids. Chlorine content in the studied MIs varies

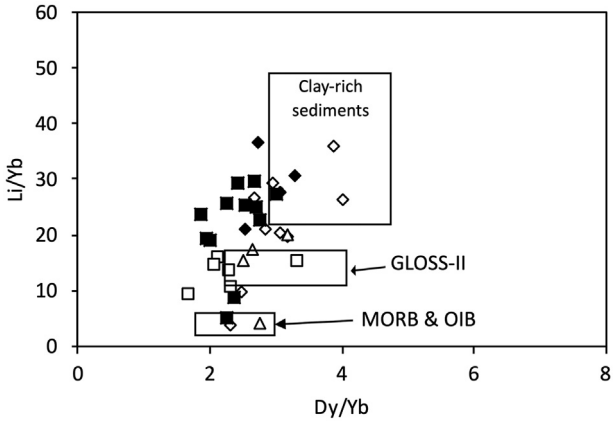

Fig. 8. Li/Yb versus Dy/Yb of melt inclusions. Measured inclusions concentration trends away MORB and OIB Sun and McDonough, 1989) toward high values of Li/Yb, exceeding the GLOSS-II (Plank 2014) composition approaching that of clay-rich sediments (Chan and Kastner 2000; Nyakiru and Koeberl, 2001).

from 416 to 1336 ppm, while Cl/K and Cl/Nb ratios range from 0.05 to 0.18 and from 11.8 to 51.2, respectively. Following the method described by Rowe and Lassiter (2009), we have explored the Cl/K and Cl/Nb variations in NVL MI. Since the bulk distribution coefficients (D) are $D_{Nb} \approx D_{Cl} < D_K$, then low degree of partial melting should increase the Cl/K in melts relatively to the mantle source, but should not significantly fractionate Cl/Nb. The resulting effect is the offset of Cl/K versus Cl/Nb ratios as observed between alkali basalts and tholeiites from Rio Grande Rift (Rowe and Lassiter 2009). A similar offset is clearly visible also in the studied MIs (Fig. 9a and b). However, since Cl, Ba and Sr are highly soluble with respect to Nb and Nd, the positive correlation of Cl/Nb or Cl/K with Ba/Nb is consistent with melt derivation from lithospheric mantle that has been modified by the interaction with subduction-derived melts or fluids (Rowe and Lassiter 2009). These trends are in accordance with the general behavior observed in MI from arc basalts, characterized by high Cl/Nb and Ba/Nb (Cervantes and Wallace 2003; Wade et al. 2006) ratios, while similar correlations are not observed in OIB and MORB lavas (Le Roux et al. 2006).

A comparison between NVL MI and those from Mt. Erebus and Ross Island magmas in Antarctica (Oppenheimer et al. 2011; Rasmussen et al. 2017), as well as with those from other geodynamic settings (MORB from East Pacific Rise; Gakkel Ridge and FAMOUS Ridge; Le Roux et al. 2006; Saal et al. 2002; Laubier et al. 2007; Shaw et al. 2010); OIB from Canary Islands and Hawaii (Longpré et al., 2017; Walowsky et al., 2019; Tucker et al. 2019); arc-related basalts (Rasmussen et al. 2018; Ruscitto et al. 2010; Roggensack et al. 1997; Wade et al. 2006; Portnyagin et al.

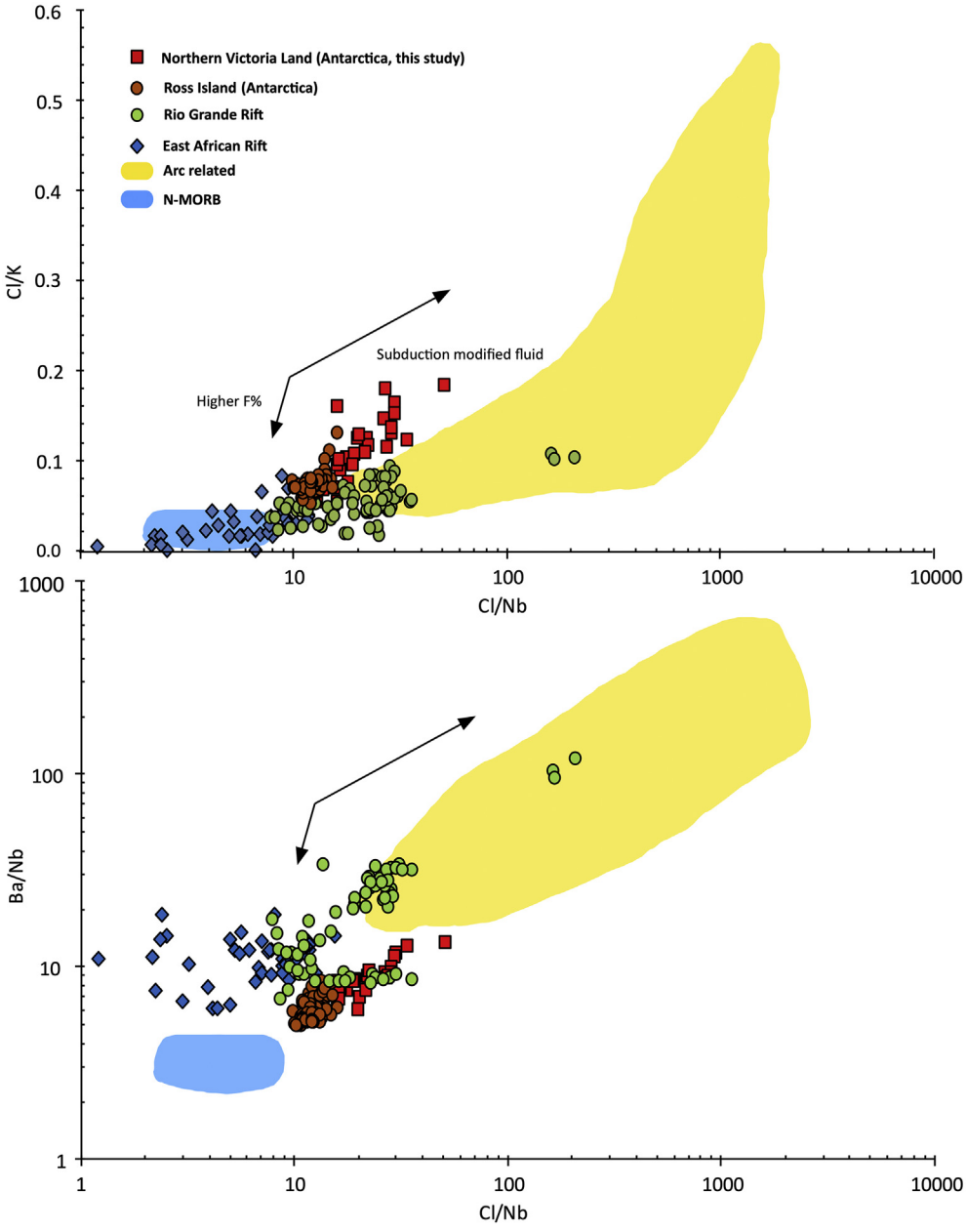

Fig. 9. Melt inclusions Cl/K and Ba/Nb versus Cl/Nb. Samples from NVL in red squares are compared with Ross Island (Mt. Erebus and Mt. Terror) samples (Oppenheimer et al. 2011; Rasmussen et al. 2017). The N-MORB field contains samples from East Pacific Rise (Le Roux et al., 2006; Saal et al. 2002), Gakkel Ridge (Shaw et al. 2010) and FAMOUS Ridge (Laubier et al. 2007), the OIB field contains analysis from Canary Islands (Longprè et al., 2007; Walowsky et al., 2019) and Hawaii (Tucker et al. 2019) while Continental Rift inclusions refer to the East African Rift and Rio Grande Rift (Hudgins et al. 2015; Rowe et al. 2015). NVL samples trend toward higher Cl/K and Ba/Nb ratios in accordance with the increasing involvement of subduction related fluids toward the ARC field which comprises basaltic melt inclusions (Cadoux et al. 2018; Rasmussen et al. 2018; Ruscitto et al. 2010; Roggensack et al. 1997; Wade et al. 2006; Portnyagin et al. 2007, 2019; Shaw et al., 2008). (For interpretation of the references to colour in this figure legend, the reader is referred to the web version of this article.)

2007; Shaw et al., 2008) and Continental Rift basalts (Hudgins et al. 2015; Rowe et al. 2015) provides interesting insights. Indeed, an almost continuous positive trend characterized by an increase of Cl/K with Cl/Nb ratio (Fig. 9a) is identifiable, with Ross Island and NVL MI plotting at the lower end of the subduction related field. Despite NVL inclusions have a significantly lower Cl/Nb and Cl/K ratio than most of arc-related melts, they show higher Cl contents with respect to other MIs from Antarctica, i.e. those from Ross Sea and Erebus magmas. More importantly, they have higher Cl values with respect to East African Rift and Rio Grande Rift melts, for whose genesis the involvement of subduction-related volatiles has been invoked (Hudgins et al. 2015; Rowe et al. 2015). Similarly, the Ba/Nb ratios (Fig. 9b) of the studied MIs show the same positive correlation with Cl/Nb that typically occurs in magma produced by mantle sources modified by arc-related fluids. Analogously, NVL inclusions have a Cl/F ratio (up to 2.64) in between the most Cl-rich MORB (up to 1.43) and arc-related values (up to 9.72).

We should reasonably hypothesize that, if the Cl enrichment in Northern Victoria Land MIs derives from the lithosphere modified by subduction-related fluids, these latters should have been introduced through metasomatism during the prolonged Ross subductive events, when NVL owned to the Paleo-Pacific active margin of Gondwana and were remobilized during the development of the West Antarctica Rift system. This hypothesis fits with the isotopic evidence of a high-μ source domain commonly recognized beneath the WARS (Aviado et al. 2015; Broadley et al. 2016; Mukasa and Dalziel 2000). The occurrence of this high $^{208}Pb/^{206}Pb$ signature, the high Nb/Th, Ce/Pb and quite low Ba/Nb and La/Nb in both lavas and MIs, together with the geochemistry of volatiles, leads to think that this enrichment in U relative to Pb occurred in the lithosphere by subduction processes over a time scales on the order of 10^8 years (Mukasa and Dalziel 2000). Further data supporting this model have been recently provided by the petrological/geodynamic study of Panter et al. (2018) and by the geochemistry of halogens and noble gases isotopes in lavas and mantle xenoliths (Broadley et al. 2016; Correale et al. 2019). These authors, in fact, highlighted how slab-derived recycled marine volatiles components, similar to marine pore fluids and serpentinites contributed to form the heterogeneous West Antarctica SCLM resulting in hydrated metasomes in veins characterized by elevated Nb, U/Pb and enriched in halogens. Variable melting of such metasomes and/or reactivation of enriched source components, which interacted with the surrounding peridotites during the Cretaceous-Cenozoic magmatism, induced the genesis of multi-stage alkaline magmatism within the WARS. The MORB like $^3He/^4He$ signature within xenoliths indicate that the NVL SCLM was further metasomatized by fluids and melts released from the asthenosphere as consequence of extension and subsequent decompression melting (Broadley et al. 2016). In this framework, the compositional variability of the studied MIs from NVL testify for the existence of melts generated by small (3%) to moderate (7%) partial melting degrees within a single SCLM domain. Our results confirm that variable melting of heterogeneously distributed amphibole-enriched domains in the peridotitic mantle (Coltorti et al. 2004) could significantly affect the composition of the produced magmas and produce basanitic to basaltic melts coexisting within a single magmatic suite.

6. Conclusions

The study of olivine-hosted MIs from Northern Victoria Land (Antarctica) allowed us to speculate about the nature and origin of volatile content of lithospheric and sub-lithospheric mantle responsible for the onset of Cenozoic magmatism as response of the formation of the Western Antarctic Rift System. The occurrence of mantle xenoliths embedded in alkaline lavas in few neighboring localities, provided an important link between lithospheric mantle and olivine-hosted MIs, permitting to quantify the budget of volatiles involved in the genesis of Cenozoic alkaline magmatism. From the measured H_2O content in nominally anhydrous minerals (NAMs) and amphibole in mantle xenoliths from Baker Rocks, we have estimated a minimum H_2O content in the mantle beneath Northern Victoria Land of about 1160 ± 436 ppm, which accounts for the measured H_2O content in primary basanitic and basaltic MI produced by a partial melting varying from 3% to 7%. Analogously, the estimated CO_2 contents in less degassed inclusions ($H_2O/(H_2O + CO_2)$ mol = 0.88–0.92) enabled us to determine a minimum content of 4400 to 8800 ppm of CO_2 in the primary basaltic and basanitic melts, leading to estimate a CO_2 content of 304 ± 64 ppm in the mantle source.

The ratio of differently fluid mobile elements as Li/Yb, Cl/K, Cl/Nb and Ba/Nb in MI led us to investigate about the possible role of arc-related fluids on the onset of Cenozoic magmatism in NVL. The observed positive correlations between these ratios suggest that the prolonged 550–110 Ma Ross subduction provided the volatiles in the lithospheric mantle together with the recycled oceanic material. This scenario would account for the settlement of heterogeneous lithospheric mantle domains, responsible for the Cenozoic magmatism. The role of old subductions in the onset of continental rifting and associated alkaline magmatism has also been proposed for the genesis of the Rio Grande Rift and East African Rift magmatism, and well fit with the diffuse HIMU component interpreted as recycled oceanic lithosphere. Nevertheless, the occurrence of the massive Jurassic Ferrar magmatic event in the Northern Victoria Land region rises some questions on how the subductive volatiles could have been retained in the mantle after the large melting event forming the Ferrar dolerite indeed justifying further studies on the volatile content and composition of both Cenozoic and Jurassic primary magmas.

Declaration of Competing Interest

The authors declare that they have no known competing financial interests or personal relationships that could have appeared to influence the work reported in this paper.

Acknowledgments

This work was funded by PRIN2017 (Piano di Ricerca di Interesse Nazionale, Italian Ministry of Education, University and Research) "Micro to macro - How to unravel the nature of the Large Magmatic Events" funded to Prof. Massimo Coltorti. Field work was made possible thanks to PNRA (Piano Nazionale Ricerca Antartide) funding and the logistic support at Mario Zucchelli Station at Terra Nova Bay. We are thankful with Raul Carampin and Leonardo Tauro (IGG-CNR, Padua, Italy) for the technical help during sample preparation and EMP analytical sessions. A special thanks to Prof. Dustin Trail and Prof. Nobu Shimizu for their priceless assistance during re-homogenization experiments and SIMS analysis of MIs. Finally, we thank Prof. Sam Mukasa and Julie Bryce for their hospitality and precious support and exiting scientific debates, to Prof. Michael Roden who edited the manuscript and two anonymous reviewers for their constructive comments.

References

Abers, G., Van Keken, P., Kneller, E.A., Ferris, A., Stachnik, J.A., 2006. The thermal structure of subduction zones constrained by seismic imaging: Implications for slab dehydration and wedge flow. Earth Planet. Sci. Lett. 3-4, 387–397. https://doi.org/10.1016/j.epsl.2005.11.055.

Arevalo, R., McDonough, W.F., 2010. Chemical variations and regional diversity observed in MORB. Chem. Geol. 271, 70–85.

Aviado, K.B., Rilling-Hall, S., Bryce, J.G., Mukasa, S.B., 2015. Submarine and Subaerial Lavas in the West Antarctic Rift System: Temporal Record of Shifting Magma Source Components from the Lithosphere and Asthenosphere. Geochemistry, Geophysics, Geosystems. https://doi.org/10.1002/2015GC006076.

Bercovici, D., Karato, S.I., 2003. Whole-mantle convection and the transition-zone water filter. Nature 425, 39–44.

Bizimis, M., Peslier, A.H., 2015. Water in Hawaiian garnet pyroxenites: implications for water heterogeneity in the mantle. Chem. Geol. 397, 61–75.

Bonadiman, C., Hao, Y., Coltorti, M., Dallai, L., Faccini, B., Huang, Y., Xia, Q., 2009. Water contents of pyroxenes in intraplate lithospheric mantle. Eur. J. Mineral. 21, 637–647.

Bonadiman, C., Nazzareni, S., Coltorti, M., Comodi, P., Giuli, G., Faccini, B., 2014. Crystal chemistry of amphiboles: implications for oxygen fugacity and water activity in lithospheric mantle beneath Victoria Land, Antarctica. Contrib. Mineral. Petrol. 167, 1–17.

Broadley, M.W., Ballentine, C.J., Chavrit, D., Dallai, L., Burgess, R., 2016. Sedimentary halogens and noble gases within Western Antarctic xenoliths: implications of the extensive volatile recycling to the sub continental lithospheric mantle. Geochim. Cosmochim. Acta 176, 139–156.

Cadoux, A., Iacono-Marziano, G., Scaillet, B., Aiuppa, A., Mather, T.A., Pyle, D.M., Deloule, E., Gennaro, E., Paonita, A., 2018. The role of melt composition on acqueous fluid v.s. silicate melt partitioning of bromine in magmas. Earth Planet. Sci. Lett. 498, 450–463.

Cartigny, P., Pineau, F., Aubaud, C., Javoy, M., 2008. Towards a consistent mantle carbon flux estimate: insights from volatile systematics (H_2O/Ce, δD, CO_2/Nb) in the North Atlantic mantle (14 N and 34 N). Earth Planet. Sci. Lett. 265, 672–685.

Casetta, F., Ickert, R.B., Mark, D.F., Bonadiman, C., Giacomoni, P.P., Ntaflos, T., Coltorti, M., 2019. The alkaline lamprophyres of the Dolomitic Area (Southern Alps, Italy): markers of the Late Triassic change from orogenic-like to anorogenic magmatism. J. Petrol. 60 (6), 1263–1298.

Casetta, F., Giacomoni, P.P., Ferlito, C., Bonadiman, C., Coltorti, M., 2020. The evolution of the mantle source beneath Mt. Etna (Sicily, Italy): from the 600 ka tholeiites to the recent trachybasaltic magmas. Int. Geol. Rev. 62 (3), 338–359. https://doi.org/10.1080/00206814.2019.1610979.

Cervantes, P., Wallace, P.J., 2003. Role of H_2O in subduction-zone magmatism: New insights from melt inclusions in high-Mg basalts from Central Mexico. Geology 31, 235–238.

Chan, L.H., Kastner, M., 2000. Lithium isotopic compositions of pore fluids and sediments in the Costa Rica subduction zone: implications for fluid processes and sediment contribution to the arc volcanoes. Earth Planet. Sci. Lett. 183, 275–290.

Chen, Y., Zhang, Y., 2008. Olivine dissolution in basaltic melt. Geochim. Cosmochim. Acta 72, 4756–4777.

Coltorti, M., Beccaluva, L., Bonadiman, C., Faccini, B., Ntaflos, T., Siena, F., 2004. Amphibole genesis via metasomatic reaction with clinopyroxene in mantle xenoliths from Victoria Land, Antarctica. Lithos 75, 115–139.

Coltorti, M., Bonadiman, C., Casetta, F., Faccini, B., Giacomoni, P.P., Pelorosso, B., Perinelli, C., 2020. Nature and evolution of the Northern Victoria Land Lithospheric Mantle (Antarctica). The Geological Society Memoir: The Antarctic Mantle. The Geological Society of, London (In press).

Correale, A., Pelorosso, B., Rizzo, A.L., Coltorti, M., Italiano, F., Giacomoni, P.P., 2019. The nature of the West Antarctic Rift System as revealed by noble gases in mantle minerals. Chem. Geol. 524, 104–118.

Cox, K.G., 1978. Flood basalts, subduction and the break-up of Gondwanaland. Nature 274, 47–49.

Dalou, C., Koga, K.T., Le Voyer, M., Shimizu, N., 2014. Contrasting partition behavior of F and Cl during mantle melting: implications for Cl/F signature in arc magmas. Prog. Earth Planet. Sci. 1.

Danyushevsky, L.V., Eggins, S.M., Fallon, T.J., 2000. H_2O abundance in depleted to moderately enriched mid-ocean ridge magmas; part I: incompatible behavior, implications for mantle storage, and origin of regional variations. J. Petrol. 41, 1329–1364.

Dasgupta, R., Hirschmann, M.M., 2010. The deep carbon cycle and melting in Earth's interior. Earth Planet. Sci. Lett. 298.

Dasgupta, R., Jackson, M.G., Lee, C., 2010. Major element chemistry of ocean island basalts — Conditions of mantle melting and heterogeneity of mantle source. Earth Planet. Sci. Lett. 289, 377–392. https://doi.org/10.1016/j.epsl.2009.11.027.

Di Genova, D., Hess, K.U., Chevrel, M.O., Dingwell, D., 2016. Models for the estimation of Fe^{3+}/Fe_{tot} ratio in terrestrial and extraterrestrial alkali- and iron-rich silicate glasses using Raman spectroscopy. Am. Mineral. 101.

Elkins-Tanton, L.T., 2007. Continental magmatism, volatile recycling, and a heterogeneous mantle caused by lithospheric gravitational instabilities. J. Geophys. Res. 112 (B3), B03405.

Giacomoni, P.P., Coltorti, M., Mollo, S., Ferlito, C., Braiato, M., Scarlato, P., 2018. The 2011-2012 paroxysmal eruptions at Mt. Etna volcano: insights on the vertically zoned plumbing system. J. Volcanol. Geotherm. Res. 349, 370–391.

Giordano, G., Lucci, F., Philips, D., 2012. Stratigraphy, geochronology and evolution of the Mt. Melbourne volcanic field (North Victoria Land, Antarctica). Bull. Volcanol. https://doi.org/10.1007/x00445-012-0643-8.

Green, D.H., 1973. Experimental melting studies on a model upper mantle composition at high pressure under water-saturated and water-undersaturated conditions. Earth Planet. Sci. Lett. 19, 37–53.

Hao, Y.T., Bonadiman, C., Coltorti, M., Xia, Q.K., 2019. Fragments of asthenosphere incorporated in the lithospheric mantle underneath the Subei Basin, eastern China; constraints from geothermobarometric results and water contents of peridotite xenoliths in Cenozoic basalts. J. Asian Earth Sci. 1, 100006.

Hauri, E.H., Gaetani, G.A., Green, T.H., 2006. Partitioning of water during melting of the Earth's upper mantle at H2O-undersaturater conditions. Earth Planet. Sci. Lett. 248, 715–734.

Hirschmann, M.M., 2018. Comparative deep Earth volatile cycles: the case for C recycling from exosphere/mantle fractionation of major (H_2O, C, N) volatiles and from H_2O/Ce, CO_2/Ba, and CO_2/Nb exosphere ratios. Earth Planet. Sci. Lett. 502, 262–273.

Hirschmann, M.M., Dasgupta, R., 2009. The H/C ratios of Earths near surface and deep reservoirs, and consequences for deep Earth volatile cycles. Chem. Geol. 262, 4–16.

Hole, M.J., LeMasurier, W.E., 1994. Tectonic controls on the geochemical composition of Cenozoic, mafic alkaline volcanic rocks from West Antarctica. Contrib. Mineral. Petrol. 117, 187–202.

Hudgins, T.R., Mukasa, S.B., Simon, A.C., Moore, G., Barifaijo, E., 2015. Melt inclusion evidence for CO_2-rich melts beneath the western branch of the East African Rift: implications for long-term storage of volatiles in the deep lithospheric mantle. Contrib. Mineral. Petrol. 169, 46.

Ivanov, A.V., Mukasa, S.B., Kamenetsky, V.S., Ackerson, M., Demonterova, E.I., Pokrovsky, B.G., Vladykin, N.V., Kolesnichenko, M.V., Litasov, K.D., Zedgeniezov, D.A., 2018. Volatile concentrations in olivine-hosted melt inclusions from meimechite and melonephelinite lavas of the Siberian Traps Large Igneous Province: evidence for flux-related high-Ti, high-Mg magmatism. Chem. Geol. 483, 443–462.

Johnson, E.R., Wallace, P.J., Cashman, K.V., Delgado Granados, H., Kent, A., 2008. Magmatic volatile contents and degassing-induced crystallization at Volcan Jorullo, Mexico: Implications for melt evolution and the plumbing systems of monogenetic volcanoes. Earth Planet. Sci. Lett. https://doi.org/10.1016/j.epsl.2008.03.004.

Keppler, H., Wiedenbeck, M., Shcheka, S.S., 2003. Carbon solubility in olivine and the mode of carbon storage in the Earth's mantle. Nature 424, 414–416.

Lachance, G.R., Trail, R.J., 1966. Practical solution to the matrix problem in X-ray analysis. Can. Spectrosc. 11, 43–48.

Lanzafame, G., Casetta, F., Giacomoni, P.P., Donato, S., Mancini, L., Coltorti, M., Ntaflos, T., Ferlito, C., 2020. The Skaros effusive sequence at Santorini (Greece): petrological and geochemical constrainst on an interplinian cycle. Lithos 362–363.

Laubier, M., Schiano, P., Doucelance, R., Ottolini, L., Laporte, D., 2007. Olivine-hosted melt inclusions and melting processes beneath the FAMOUS zone (Mid-Atlantic Ridge). Chem. Geol. 240, 129–150.

Le Bas, M.J., Le Maitre, R.W., Streckeisen, A., Zanettin, B., 1986. A chemical classification of volcanic rocks based on the total alkali-silica diagram. J. Petrol. 27, 745–750.

Le Roux, P.J., Shirey, S.B., Hauri, E.H., Perfit, M.R., Bender, J.F., 2006. The effects of variable sources, processes and contaminants on the composition of northern EPR MORB (8–108 and 12–148N): evidence from volatiles (H_2O, CO_2, S) and halogens (F, Cl). Earth Planet. Sci. Lett. 251, 209–231.

Le Vojer, M., Kelley, K.A., Cottrell, E., Hauri, E.H., 2017. Heterogeneity in mantle carbon content from CO2-undersaturated basalts. Nature Comm. https://doi.org/10.1038/ncomms14062.

Liu, X.M., Rudnick, R.L., 2011. Constraints on the continental crustal mass loss via chemical weathering using lithium and its isotopes. Proc. Natl. Acad. Sci. U. S. A. 108 (52), 20873–20880.

Longpré, M.A., Stix, J., Klugel, A., Shimizu, N., 2017. Mantle to surface degassing of carbon- and sulphur-rich alkaline magma at el El Hierro, Canary Islands. Earth Planet. Sci. Lett. 460, 268–280.

Marty, B., 2012. The origins and concentrations of water, carbon, nitrogen and noble gases on Earth. Earth Planet. Sci. Lett. 313–314, 56–66.

Marty, B., Zimmermann, L., 1999. Volatiles (He, C, N, Ar) in mid-ocean ridge basalts: assessment of shallow-level fractionation and characterization of source composition. Geochim. Cosmochim. Acta 63, 3619–3633.

McDonough, W.F., Sun, S.S., 1995. The composition of the Earth. Chem. Geol. 120, 223–253.

Danyushevsky, L.V., McNeill, A.W., Sobolev, A.V., 2002. Experimental and petrological studies of melt inclusions in phenocrysts from mantle-derived magmas: an overview of techniques, advantages and complications. Chem. Geol. 183, 5–24.

Melchiorre, M., Coltorti, M., Bonadiman, B., Faccini, B., O'Reilly, S.Y., Pearson, N., 2011. The role of eclogite in the rift-related metasomatism and Cenozoic magmatism of northern Victoria Land, Antarctica. Lithos 124, 319–330.

Michael, P., 1995. Regionally distinctive sources of depleted MORB: evidence from trace elements and H_2O. Earth Planet. Sci. Lett. 131, 301–320.

Miller, W.G.R., Maclennan, J., Shorttle, O., Gaetani, G.A., Le Roux, V., Klein, F., 2019. Estimating the carbon content of the deep mantle with Icelandic melt inclusions. Earth Planet. Sci. Lett. 523, 115699.

Mollo, S., Giacomoni, P.P., Andronico, D., Scarlato, P., 2015. Clinopyroxene and titanomagnetite cation redistributions at Mt. Etna volcano (Sicily, Italy): footprints of final solidification history of lava fountains and lava flows. Chem. Geol. https://doi.org/10.1016/j.chemgeo.2015.04.017.

Mukasa, S.B., Dalziel, I.W.D., 2000. Marie Byrd Land, West Antarctica: evolution of Gondwana's Pacific margin constrained by zircon U-Pb geochronology and feldspar common-Pb isotopic compositions. Bull. Geol. Soc. Am. 112 (4), 611–627.

Nardini, I., Armienti, P., Rocchi, S., Dallai, L., Harrison, D., 2009. Sr–Nd–Pb–He–O isotope and geochemical constraints on the genesis of Cenozoic magmas from the West Antarctic Rift. J. Petrol. 50, 1359–1375.

Newman, S., Lowenstern, J.B., 2002. VolatileCalc: a silicate melt-H_2O-CO_2 solution model written in Visual Basic for Excel. Comput. Geosci. 28, 597–604.

Novella, D., Frost, D.J., Hauri, E.H., Bureau, H., Raepsaet, C., Roberge, M., 2014. The distribution of H_2O between silicate melt and nominally anhydrous peridotite and the onset of hydrous melting in the deep upper mantle. Earth Planet. Sci. Lett. 400, 1–13.

Nyakairu, G.W.A., Koeberl, C., 2001. Mineralogical and chemical composition and distribution of rare earth elements in clay-rich sediments from central Uganda. Geochem. J. 35, 13–28.

Oppenheimer, C., Moretti, R., Kyle, P.R., Eschenbacher, A., Lowenstern, J.B., Hervig, R.L., Dunbar, N.W., 2011. Mantle to surface degassing of alkalic magmas at Erebus volcano, Antarctica. Earth Planet. Sci. Lett. 306, 261–271.

Ottolini, L., Camara, F., Hawthorne, F.C., Stirling, J., 2002. SIMS matrix effects in the analysis of light elements in silicate minerals: comparison with SREF and EMPA data. Am. Mineral. 87, 1477–1485.

Panter, K.S., Castillo, P., Krans, S., Deering, C., McIntosh, W., Valley, J.W., Blusztajn, J., 2018. Melt origin across a rifted continental margin: a case for subduction-related metasomatic agents in the lithospheric source of alkaline basalt, NW Ross Sea, Antarctica. J. Petrol. 59 (3), 517–558.

Panter, K.S., Hart, S.R., Kyle, P.R., Blusztanjn, J., Wilch, T.I., 2000. Geochemistry of Late Cenozoic basalts from the Crary Mountains: Characterization of mantle sources in Marie Byrd Land, Antarctica. Chem. Geol 165, 215–241.

Papale, P., Moretti, R., Barbato, D., 2006. The compositional dependence of the saturation surface of $H_2O + CO_2$ fluids in silicate melts. Chem. Geol. 229, 78–95.
Pelorosso, B., Bonadiman, C., Coltorti, M., Faccini, B., Melchiorre, M., Ntaflos, T., Gregoire, M., 2016. Pervasive, tholeiitic refertilisation and heterogeneous metasomatism in Northern Victoria Land lithospheric mantle (Antarctica). Lithos 248–251, 493–505.
Pelorosso, B., Bonadiman, C., Coltorti, M., Melchiorre, M., Giacomoni, P.P., Ntaflos, T., Gregoire, M., Benoit, M., 2017. Role of Percolating Melts in Antarctic Subcontinental Lithospheric Mantle: New Insights from Handler Ridge Mantle Xenoliths (Northern Victoria Land, Antarctica). The Geological Society of America, Special Paper 526.
Perinelli, C., Orlando, A., Conte, A.M., Armienti, P., Borrini, P., Faccini, B., Misiti, V., 2008. Metasomatism induced by alkaline magma on upper mantle of the Northern Victoria Land (Antarctica): an experimental approach. In: Coltorti, M., Gregoire, M. (Eds.), Mantle Metasomatism in Intra-Plate and Suprasubduction Settings. Geological Society vol. 293. Special Publications, London, pp. 197–221.
Pilet, S., Baker, M., Stolper, E., 2008. Metasomatized lithosphere and the origin of alkaline lavas. Science 320, 916–919.
Plank, T., 2014. The chemical composition of subducting sediments. Treatise Geochem. 4, 607–629.
Portnyagin, M., Hoernle, K., Plechov, P., Mironov, N., Khbunaya, S., 2007. Constraints on mantle melting and composition and nature of slab components in volcanic arcs from volatiles (H_2O, S, Cl, F) and trace elements in melt inclusions from the Kamchatka Arc. Earth Planet. Sci. Lett. 225, 53–69.
Portnyagin, M., Mironov, N., Gurenko, A., Almeev, R.R., Luft, C., Holtz, F., 2019. Dehydration of melt inclusions in olivine and implications for the origin of silica-undersaturated island-arc melts. Earth Planet. Sci. Lett. 517, 95–105. https://doi.org/10.1016/j.epsl.2019.04.021.
Rasmussen, D.J., Kyle, P.R., Wallace, P.J., Sims, K.W.W., Gaetani, G.A., Phillips, E.H., 2017. Understanding degassing and transport of CO_2-rich alkali magmas at Ross Island, Antarctic using olivine-hosted melt inclusions. J. Petrol. 5, 841–862.
Rasmussen, D.J., Plank, T.A., Roman, D.C., Powerm, J.A., 2018. When does eruption run-up begin? Multidisciplinary insight from the 1999 eruption of Shishaldin volcano. Earth Planet. Sci. Lett. 408, 1–14.
Robey, W.W., 1951. Geologic history of sea water: an attempt to state the problem. Bull. Geol. Soc. Am. 62, 1111–1148.
Rocchi, S., Armienti, P., D'Orazio, M., Tonarini, S., Wijbrans, J.R., Di Vincenzo, G., 2002. Cenozoic magmatism in the western Ross Embayment: Role of mantle plume versus plate dynamics in the development of the West Antarctic Rift System. J. Geophys. Res. Solid Earth 107 (B9). https://doi.org/10.1029/2001JB000515.
Roeder, P.L., Emslie, R.F., 1970. Olivine-liquid equilibrium. Contrib. Mineral. Petrol. 29, 275–289.
Roggensack, K., Hervig, R.L., McKnight, S.B., Williams, S.N., 1997. Explosive basaltic volcanism from Cerro Negro Volcano: influence of volatiles on eruptive style. Science 277, 1639–1642.
Rosenthal, A., Hauri, E.H., Hirschmann, M.M., 2015. Experimental determination of C, F, and H partitioning between mantle minerals and carbonated basalt, CO_2/Ba and CO_2/Nb systematics of partial melting, and the CO_2 contents of basaltic source regions. Earth Planet. Sci. Lett. 412, 77–87.
Rowe, M.C., Lassiter, J.C., 2009. Chlorine enrichment in central Rio Grande Rift basaltic melt inclusions: evidence for subduction modification of the lithospheric mantle. Geology 37, 439–442.
Rowe, M.C., Lassiter, J.C., Goff, K., 2015. Basalt volatile fluctuations during the continental rifting: an example from the Rio Grande Rift, USA. Geochem. Geophys. Geosyst. https://doi.org/10.1002/2014GC005648.
Ruscitto, D.M., Wallace, P.J., Johnson, E.R., Kent, A.J.R., Binderman, I.N., 2010. Volatile contents of mafic magmas from cinder cones in the Central Oregon High Cascades: implications for magma formation and mantle conditions in a hot arc. Earth Planet. Sci. Lett. 298, 153–161.
Saal, A.E., Hauri, E.H., Langmuir, C.H., Perfit, M.R., 2002. Vapor undersaturation in primitive mid-ocean-ridge basalt and the volatile content of Earth's upper mantle. Nature 419, 451–455.
Salters, V., Stracke, A., 2004. Composition of the depleted mantle. Geochem. Geophys. Geosyst. 5.
Salvini, F., Brancolini, G., Busetti, M., Storti, F., Mazzarini, F., Coren, F., 1997. Cenozoic geodynamics of the Ross Sea region, Antarctica: Crustal extension, intraplate strike-slip faulting, and tectonic inheritance. J. Geophys. Res. Solid Earth 102, 24669–24696.
Schilling, J., Bergeron, M., Evans, R., 1980. Halogens in the Mantle Beneath the North Atlantic. Philos. Trans. R. Soc. Lond. Ser. A Math. Phys. Sci. 297 (1431), 147–178.
Shaw, D.M., 1979. Trace element melting models. Phys. Chem. Earth 11, 577–586.
Shaw, A.M., Hauri, E.H., Fischer, T.P., Hilton, D.R., Kelley, K.A., 2008. Hydrogen isotopes in Mariana arc melt inclusions: implications for subduction dehydration and the deep-Earth water cycle. Earth Planet. Sci. Lett. 275, 138–145.
Shaw, A., Behn, M.D., Humphreis, S.E., Sohn, R.A., Gregg, P.M., 2010. Deep pooling of low degree melts and volatile fluxes at the 85°E segment of the Gakkel Ridge: evidence from olivine-hosted melt inclusions and glasses. Earth Planet. Sci. Lett. 289, 311–322.
Shcheka, S.S., Wiedenbeck, M., Frost, D.J., Keppler, H., 2006. Carbon solubility in mantle minerals. Earth Planet. Sci. Lett. 245, 730–742.
Stefano, C.J., Mukasa, S.B., Andronikov, A., Leeman, W.P., 2011. Water and other volatile systematics of olivine-hosted melt inclusions from the Yellowstone hotspot track. Contrib. Mineral. Petrol. 161 (4), 615–633.
Sun, S.S., McDonough, W.D., 1989. Chemical and isotopic systematics of oceanic basalts: Implications for mantle composition and processes in Saunders, A.D., and Norry, M.J., eds., Magmatism in the ocean basins. Geol. Soc. London Spec. Pub. 42, 313–345.
Taracsak, Z., Hartley, M.E., Burgess, R., 2019. High fluxes of deep volatiles from ocean island volcanoes: insights from El Hierro, Canry Islands. Geochim. Cosmochim. Acta 258.
Trail, D., Bruce Watson, E., Tailby, N.D., 2012. Ce and Eu anomalies in zircon as proxies for the oxidation state of magmas. Geochim. Cosmochim. Acta 97, 70–87.
Tucker, J.M., Hauri, E.H., Pietruszka, A.J., Garcia, M.O., Marske, J.P., Trusdell, F.A., 2019. A high carbon content of the Hawaiian mantle from olivine-hosted melt inclusions. Geochim. Cosmochim. Acta 254, 156–172.
Wade, J.A., Plank, T., Melson, W.G., Soto, G.J., Hauri, E.H., 2006. Volatile content of magmas from Arenal volcano, Costa Rica. J. Volcanol. Geotherm. Res. 157, 94–120.
Walowsky, K.J., Kirsten, L.A., De Hoog, J.C.M., Elliott, T.R., Savov, I.P., Jones, R.E., 2019. Investigating ocan island mantle source heterogeneity with boron isotopes in melt inclusions. Earth Planet. Sci. Lett. 508, 97–108.
Workman, R.K., Hart, S.R., 2005. Major and trace element composition of the depleted MORB mantle (DMM). Earth Planet. Sci. Lett. 231, 53–72.
Wörner, G., 1999. Lithospheric dynamics and mantle sources of alkaline magmatism of the Cenozoic West Antarctic Rift System. Glob. Planet. Chang. 23, 61–77.
Zellmer, G.F., Edmonds, M., Straub, M.E., 2014. Volatiles in subduction zone magmatism. In: Zellmer, G.F., Edmonds, M., Straub, S.M. (Eds.), The Role of Volatiles in the Genesis, Evolution and Eruption of Arc Magmas. Geol. Soc. 410. Special Publications, London. https://doi.org/10.1144/SP410.13.
Zhang, Y.X., Stolper, E.M., 1991. Water diffusion in a Basaltic Melt. Nature 351, 306–309.